Cortical hyperexcitability in mouse models and patients with amyotrophic lateral sclerosis is linked to noradrenaline deficiency.

Authors:

Jelena Scekic-Zahirovic[1,†,‡], Cristina Benetton[2,‡], Aurore Brunet[1,‡], XiaoQian Ye[3,4], Evgeny Logunov[3,4], Vincent Douchamps[5], Salim Megat[1], Virginie Andry[6], Vanessa Wing Yin Kan[3,4], Geoffrey Stuart-Lopez[1], Johan Gilet[1], Simon J Guillot[1], Sylvie Dirrig-Grosch[1], Charlotte Gorin[1], Margaux Trombini[1], Stéphane Dieterle[1], Jérôme Sinniger[1], Mathieu Fischer[1], Frédérique René[1], Zeynep Gunes[3,4], Pascal Kessler[7], Luc Dupuis[1], Pierre-François Pradat[2,8], Yannick Goumon[6], Romain Goutagny[5], Véronique Marchand-Pauvert[2,§,*], Sabine Liebscher[3,4,, 9, 10,§,*] & Caroline Rouaux[1,§,*].

Affiliations:

[1] Université de Strasbourg, Inserm UMRS 1329, Strasbourg Translational Neuroscience and Psychiatry (STEP), Centre de Recherche en Biomédecine de Strasbourg, 1 rue Eugène Boeckel, 67 000 Strasbourg, France.

† Present address: German Center for Neurodegenerative Diseases (DZNE), Ulm, Germany.

[2] Sorbonne Université, Inserm, CNRS, Laboratoire d'Imagerie Biomédicale, LIB, 75006 Paris, France.

[3] Institute of Clinical Neuroimmunology, Klinikum der Universität München, Ludwig - Maximilians University Munich, 82152 Martinsried, Germany.

[4] Biomedical Center, Ludwig - Maximilians University Munich, 82152 Martinsried, Germany.

[5] Laboratoire de Neurosciences Cognitives et Adaptatives (LNCA), Université de Strasbourg, Faculté de Psychologie, 12 rue Goethe, 67000 Strasbourg, France; LNCA, UMR 7364, CNRS, 12 rue Goethe, 67000 Strasbourg, France.

[6] CNRS UPR3212, SMPMS-INCI, Mass Spectrometry Facilities, Institut des Neurosciences Cellulaires et Intégratives, Centre National de la Recherche Scientifique and University of Strasbourg, 67 000 Strasbourg, France.

[7] Inserm UMS 38, Centre de Recherche en Biomédecine de Strasbourg, Faculté de Médecine, Université de Strasbourg, 67 000 Strasbourg, France.

[8] Neurologie, AP-HP, Hôpital Pitié-Salpêtrière, 75013-Paris, France.

[9] Munich Cluster for Systems Neurology (SyNergy), 81377 Munich, Germany.

[10] University of Cologne, Medical Faculty & University hospital of Cologne, Dept. of Neurology, Cologne, 50937 Germany

‡ These authors contributed equally to this work.

§ These authors jointly supervised this work: Véronique Marchand-Pauvert, Sabine Liebscher, Caroline Rouaux.

*Corresponding authors: veronique.marchand-pauvert@inserm.fr ; sabine.liebscher@med.uni-muenchen.de ; caroline.rouaux@inserm.fr

One Sentence Summary

Cortical dysfunction in ALS manifests in altered theta-gamma coupling that correlates with disease progression and relies on noradrenergic deficits.

OVERLINE: NEURODEGENERATIVE DISEASE

Editor's Summary

Abstract

Amyotrophic lateral sclerosis (ALS) is a devastating neurodegenerative disease, characterized by the death of upper (UMN) and lower motor neurons (LMN) in the motor cortex, brainstem and spinal cord. Despite decades of research, ALS remains incurable, challenging to diagnose, and of extremely rapid progression. A unifying feature of sporadic and familial forms of ALS is cortical hyperexcitability, which precedes symptom onset, negatively correlates with survival, and is sufficient to trigger neurodegeneration in rodents. Using electrocorticography in the $Sod1^{G86R}$ and $Fus^{\Delta NLS/+}$ ALS mouse models, and standard electroencephalography recordings in patients with sporadic ALS, we demonstrate a deficit in theta-gamma phase-amplitude-coupling (PAC) in ALS. In mice, PAC deficits started before symptom onset, and in patients, PAC deficits correlated with the rate of disease progression. Using mass spectrometry analyses of CNS neuropeptides, we identified a presymptomatic reduction of noradrenaline (NA) in the motor cortex of ALS mouse models, further validated by in vivo two-photon imaging in behaving $SOD1^{G93A}$ and $Fus^{\Delta NLS/+}$ mice, that revealed pronounced reduction of locomotion-associated NA release. NA deficits were also detected in post-mortem tissues from patients with ALS, along with transcriptomic alterations of noradrenergic signalling pathways. Pharmacological ablation of noradrenergic neurons with DSP-4 reduced theta-gamma PAC in wildtype mice and administration of a synthetic precursor of NA augmented theta-gamma PAC in ALS mice. Our findings suggest theta-gamma PAC as means to assess and monitor cortical dysfunction in ALS and warrant further investigation of the NA system as a potential therapeutic target.

INTRODUCTION

The neurodegenerative disease amyotrophic lateral sclerosis (ALS) is primarily characterized by the death of upper (UMN) and lower motor neurons (LMN) in the motor cortex and bulbo-spinal segments, respectively *(1)*. ALS is mostly a sporadic disease, but about 10% of the cases have a family history, two third of which arise from mutations in *C9ORF72*, *SOD1*, *TARDBP* and *FUS* genes *(2)*. Due to the lack of effective treatments, the disease is fatal within only 2-5 years upon symptom onset *(2)*. ALS diagnosis is often complicated due to clinical heterogeneity and the fact that UMN signs are more difficult to detect and can be masked by LMN signs *(1)*, which greatly delays treatment initiation and limits inclusion in clinical trials. A large body of evidence, however, clearly demonstrates early motor cortex impairment in ALS *(3, 4)*. A systematic investigation of cortical dysfunction thus bears the great potential for speeding up diagnosis and offering critical insight into pathogenesis.

Cortical impairment in ALS is associated with cortical hyperexcitability, which has been documented in sporadic and familial forms of ALS *(5-7)*. It was shown to precede motor symptom onset in *SOD1* mutation carriers and sporadic ALS cases and to correlate with disease severity/progression *(5)*. Indeed, a corticofugal disease trajectory, in which the pathology is initiated in the cortex and spreads along anatomical projections to subcortical regions was proposed *(3)*. Recent studies in rodents further substantiate this notion. Chronic chemogenetic stimulation of parvalbumin-positive interneurons in the motor cortex of $SOD1^{G93A}$ mice decreases UMN hyperexcitability and downstream MN degeneration, and increases mouse survival *(8)*. Furthermore, cytoplasmically mislocalized TDP-43 in UMN of wild-type mice is sufficient to render them hyperexcitable and to induce the degeneration of downstream MN *(9)*.

Cortical hyperexcitability in ALS patients has been thus far mainly assessed by using the gold standard paired-pulse transcranial magnetic stimulation (ppTMS) combined with electromyography (EMG) *(5)*. However, the technique is often limited to the assessment of upper limb innervation, hinges critically on functional UMN-to-LMN and LMN-to-muscle connections, and can therefore not be implemented throughout disease progression as neurodegeneration progresses. For the same reason, implementations in rodent models, which recapitulate UMN and LMN degeneration *(6, 7)*, are hampered. Therefore, alternatives to ppTMS are needed to easily and reliably assess cortical dysfunction. Electroencephalography (EEG) in patients and electrocorticography (ECoG) in rodents offer these advantages through the investigation of brain oscillations and their interactions, without the need for LMN involvement. A phenomenon probed in cortical EEG is cross-frequency coupling, and in particular phase-amplitude frequency coupling (PAC), which refers to the modulation of the amplitude of a fast oscillation by the phase of a slow oscillation *(10)*. Cross-frequency coupling in general and PAC in particular are seen as a means to coordinate neural activity across different spatial and temporal scales, through the interaction between large-scale brain networks that oscillate and synchronize at lower frequencies (delta, theta, alpha, beta

bands) and fast, local networks that are active at higher frequencies and required for effective computation and synaptic modification (gamma band) *(11)*. In the neocortex, coupling has been reported between the amplitude of broadband gamma activity (>30Hz), and the phase of low-frequency rhythms, including delta (0.5-4Hz), theta (4-8Hz) and alpha (8-13Hz) *(11)*. Importantly, PAC is highly dependent on proper excitation/inhibition balance *(11, 12)*, and was shown to be compromised in neurodegenerative disorders, such as Parkinson's disease (PD) *(13, 14)*, Alzheimer's disease (AD) *(15-18)*, and in frontotemporal dementia (FTD) *(19)*. To our knowledge, PAC has not yet been investigated in ALS patients.

Despite evidence for its contribution to ALS pathophysiology in patients and rodent models *(5, 8, 9)*, the cellular and molecular mechanisms underlying cortical hyperexcitability and MN degeneration remain incompletely understood. Clinical ppTMS studies have revealed increased excitation and compromised inhibition, indicating circuit-level deficits *(5)*. Preclinical studies have demonstrated early postnatal synaptic deficits in *SOD1*^{G93A} and *TDP-43*^{Q331K} transgenic mice, increased excitation onto UMNs, and increased excitability of cortical neurons in the *Sod1*^{G93A}, *TDP-43*^{A315T} *(6, 7)* and *Fus*$^{\Delta NLS/+}$ *(20)* mouse models of the disease. In addition, several lines of evidence indicate an involvement of cell types other than UMN, such as inhibitory interneurons *(8)* or glia cells *(21, 22)*, arguing for more complex network changes. However, in addition to the main neurotransmitters, glutamate and GABA, other neurotransmitters and neuromodulators contribute to the fine tuning of motor cortex activity, which are less well studied *(6, 23)*. These comprise amongst others serotonin, whose homeostasis is impaired in patients with ALS patients and mouse model of the disease *(24, 25)*, dopamine, which is prominently altered in PD *(26)* and noradrenaline (NA), impaired in PD and AD *(27, 28)*. Given the compelling evidence for an involvement of neuromodulators in the pathophysiology of other neurodegenerative diseases, we here hypothesized that they also play a role in ALS.

Employing ECoG and EEG recordings in mice and humans respectively, in vivo two-photon imaging in behaving mice, liquid-chromatography-mass spectrometry, histology and transcriptomics of human and mouse tissue, we here show that deficits in PAC are a traceable phenomenon in ALS patients and mouse models which was associated with cortical NA deficits. We also show that NA reduction can be successfully targeted pharmacologically, which acutely mitigates cortical hyperexcitability in mice.

RESULTS

Sod1^{G86R} *and Fus*$^{\Delta NLS/+}$ *mice display increased susceptibility to pentylenetetrazol*

We first wanted to investigate whether the cortical hyperexcitability described in patients with ALS translates into broader cortical network dysfunction and cortical hyperexcitability in ALS mouse models. To address these questions, we chose the BAC transgenic *Sod1*^{G86R} mouse model of ALS, maintained on the FVB/N background *(29)*, and the knock-in *Fus*$^{\Delta NLS/+}$ mouse model of ALS and FTD, maintained on the C57Bl/6J background *(30)*, for their genetic and phenotypic complementarity. Transgenic mice

overexpressing a mutant murine *Sod1*^{G86R} gene, present with initial loss of UMN by 60 days, muscle denervation and progressive motor impairments by 90 days, followed by ultimate LMN degeneration and death of the animals by 105-120 days of age *(29, 31)* (**Fig. 1, A**). Knock-in *Fus*$^{\Delta NLS/+}$ mice instead express a truncated form of *Fus* in one of the two endogenous alleles, and display spontaneous hyperactivity by 4 months and mild motor impairments along with cognitive and behavioural deficits by 10 months of age *(20, 30)* (**Fig. 1, B**). We first submitted *Sod1*^{G86R} and *Fus*$^{\Delta NLS/+}$ to the Pentylenetetrazol (PTZ) susceptibility test, using ECoG (**Fig. 1, A to C**). PTZ is a non-competitive $GABA_A$ receptor antagonist used to unravel network hyperexcitability in animal models of epilepsy and neurodegeneration *(32, 33)*. We administered a single subconvulsive dose of PTZ (30mg/kg) to 85-day-old *Sod1*^{G86R} and 4-month-old *Fus*$^{\Delta NLS/+}$ animals and respective wild-type (WT) littermates. All injected animals arrested their behaviour without any overt tonic-clonic seizures. We then computed the number of epileptiform-like events in ECoG traces prior to and after PTZ injection (**Fig. 1, D to I**). In *Sod1*^{G86R} animals, we found significantly increased number of events ($p<0.0001$, **Fig. 1, F**) and decreased latency to the first event ($p=0.0043$, **Fig. 1, G**), compared to their WT littermates. We observed the same results in *Fus*$^{\Delta NLS/+}$ mice, with significantly increased number of events ($p=0.03025$, **Fig. 1, H**), and decreased latency ($p=0.0037$, **Fig. 1, I**), compared to WT littermates. Of note, mice on the FVB/N background displayed a greater response to PTZ than mice on the C57Bl/6J background, in accordance with former reports *(34, 35)*. These results indicate that *Sod1*^{G86R} and *Fus*$^{\Delta NLS/+}$ mouse models of ALS display cortical network hyperexcitability, revealed by increased susceptibility to PTZ.

Sod1*^{G86R} *and Fus*$^{\Delta NLS/+}$ *mice display impaired theta-gamma PAC

To longitudinally assess cortical network dysfunction in mouse models of ALS, we further employed ECoG recordings to conduct phase-amplitude coupling (PAC) analyses (**Fig. 2, A**). Theta-gamma PAC is highly dependent on proper excitation/inhibition balance *(11, 12)*, with gamma frequency synchrony attributed to interconnected fast-spiking $GABA_A$-expressing interneurons *(11)*, and theta frequency attributed to the cortical excitatory neurons, and more particularly to layer V pyramidal neurons of the human brain *(36, 37)*. In addition, rodent and human motor cortices were reported to exhibit strong theta-gamma coupling *(38-40)*. To assess PAC, we chose the method of the Modulation Index (MI) developed by Adriano B. L. Tort, for its noise tolerance and amplitude independence *(41, 42)*. We ran longitudinal ECoG recordings from subdural electrodes positioned over the sensorimotor areas (**Fig. 1, C**) and performed PAC analyses, in rapid eye movement (REM) sleep (**Fig. 2**) and active wakefulness (**Fig. 3**), two states known to display theta-gamma PAC in rodents *(43)*, from the presymptomatic stage (45 days) until disease end-stage (105 days) in *Sod1*^{G86R} mice, and from presymptomatic (3 months) to symptomatic (11 months) stages in *Fus*$^{\Delta NLS/+}$ mice. As expected during REM sleep, comodulograms displayed coupling between theta and low

gamma (T-LG, around 60Hz) and theta and high gamma (T-HG, around 120Hz) (**Fig. 2, B and C**). At the earliest recorded ages, *Sod1*^{G86R} and *Fus*$^{\Delta NLS/+}$ animals demonstrated impaired theta gamma PAC during rapid eye movement (REM) sleep (**Fig. 2, D and E**). T-LG PAC was differentially affected in the two mouse lines. Whereas the MI was significantly decreased in the *Sod1*^{G86R} (**Fig. 2, F**, genotype effect: p=0.0073 in mixed-effect analysis), it was not altered in the *Fus*$^{\Delta NLS/+}$ animals (**Fig. 2, G**). T-HG PAC instead was significantly decreased in both mouse lines (**Fig. 2, H and I**; genotype effect: p=0.0007 for *Sod1*^{G86R} and 0.0039 for *Fus*$^{\Delta NLS/+}$ in mixed-effect analysis), from the first recordings, and remained as such throughout the disease course. Power spectrum analysis revealed that LG and HG powers were unaffected in both lines (**fig. S1, A to D**). Theta power was significantly decreased in *Sod1*^{G86R} animals (**fig, S1, E,** genotype effect: p=0.0009 in mixed-effect analysis) but remained unchanged in *Fus*$^{\Delta NLS/+}$ mice (**fig. S1, F**). Similarly total power was significantly decreased in *Sod1*^{G86R} animals (**fig, S1, G,** genotype effect: p=0.0028 in mixed-effect analysis) and unchanged in *Fus*$^{\Delta NLS/+}$ mice (**fig. S1, H**), ruling out the possibility that the decreased T-HG PAC revealed in both mouse lines during REM sleep, was solely due to a power effect. We further analysed theta-gamma PAC during active wakefulness (**Fig. 3**). As expected for this state of vigilance *(43)*, comodulograms displayed only T-LG PAC (**Fig. 3, A and B**), with lower MIs compared to REM sleep. At the first recorded ages, we found a decrease of the MI corresponding to LG frequencies in *Sod1*^{G86R} animals (**Fig. 3, C**) but not in the *Fus*$^{\Delta NLS/+}$ mice (**Fig. 3, D**). Decreased MI was maintained throughout the whole disease duration in *Sod1*^{G86R} mice (**Fig. 3, E,** genotype effect: p=0.0004 in mixed-effect analysis) but remained unchanged in the *Fus*$^{\Delta NLS/+}$ animals compared to controls (**Fig. 3, F**). Decreased T-LG PAC in the *Sod1*^{G86R} line was accompanied by decreased total and theta powers (**fig. S2, A and B**, genotype effect: p=0.0022 and 0.0012 respectively in mixed-effect analysis), but LG and HG powers remained unaffected (**fig. S2, C and D**). In *Fus*$^{\Delta NLS/+}$ mice, powers remained unchanged except for LG power that was decreased (**fig. S2, E to H,** genotype effect: p=0.0112 in mixed-effect analysis**)**. Together, the data reveal that *Sod1*^{G86R} and *Fus*$^{\Delta NLS/+}$ animals present with common altered cortical network function that translates into decreased T-HG PAC during REM sleep. In addition, the *Sod1*^{G86R} mouse model of ALS also presents with decreased T-LG PAC during both REM sleep and active wakefulness, prompting us to test whether such a phenotype could be observed in ALS patients during wakefulness.

Patients with sporadic ALS display impaired theta-gamma PAC in resting state

We performed resting state EEG (rsEEG) recordings and theta-gamma PAC analyses (**Fig. 4, A**) on 26 patients with sporadic ALS (**Table 1**) and an age- and sex-matched group of 26 healthy individuals, focusing on the motor cortex *(38-40)*. Electrodes were located above the sensorimotor areas (C_3 and C_4) and the interhemispheric sulcus (F_z, C_z and P_z) that can also capture EEG signals from neighbouring motor cortex, and recording performed on every participant successively with eyes open (EO) and eyes closed

(EC). We generated comodulograms for each of the five electrodes of both patients and controls, in both the EO and EC conditions (**Fig. 4, B**), and extracted the mean MI for each condition (**Fig. 4, C**). To evaluate the influence of *i)* the recording condition (EO *vs.* EC), *ii)* the recording site (channels) and *iii)* the group affiliation (Controls vs. ALS), we built a repeated-measures linear mixed-effect model (rmLMM). The analysis revealed that theta-gamma PAC was significantly stronger in the EO compared to the EC condition ($p<0.0001$, **fig. S3, A, Fig. 4, C**), that the recording site presented a significant influence ($p<0.0001$, **fig. S3, B**), and that theta-gamma PAC was significantly lower in ALS patients compared to Controls ($p=0.0043$, **fig. S3, C, Fig. 4, C**). *Post-hoc* analysis further revealed a significant decrease of theta-gamma PAC in ALS patients both in the EO and EC conditions ($p=0.0133$ and 0.0194 respectively, **Fig. 4, C**), driven by a selective effect at the level of C_3 ($p=0.0061$ and <0.0001 in the EO and EC conditions, respectively, **Fig. 4, C**). The signal power in the theta and gamma bands, as well as the absolute power, were not statistically different between controls and ALS patients (**fig. S3, D to F**), ruling out the possibility that decreased theta-gamma PAC arose from altered powers. We further focused our analysis on the C_3 channel in the EC condition that showed the stronger effect (reduced by 63.83% in ALS patients compared to controls, $p<0.0001$), and tested whether EC C_3 theta-gamma PAC correlated with the main clinical features of ALS patients. We found no correlation between the patient's mean MI and site of onset ($p=0.9572$, **fig. S4, A**), UMN score ($p=0.8033$ **fig. S4, B**), ALSFRS-r ($p=0.0535$, **fig. S4, C**), or disease duration ($p=0.3822$, **fig. S4, D**). However, patients' EC C_3 theta-gamma PAC significantly correlated with the disease progression rate ($p=0.0323$, **Fig. 4, D**). No correlation was found between the absolute power measured of C_3 in the EC condition and the main clinical features (**fig. S4, E to I**). Finally, stratification of patients into slow and fast progressors (**Table 1**) confirmed that fast progressors displayed a significantly lower EC C_3 theta-gamma PAC than the slow progressors ($p=0.0265$, **Fig. 4, E**). Together, the data indicate that theta-gamma PAC, recorded in EC conditions over the left sensorimotor area is significantly decreased in sporadic ALS patients compared to healthy controls, and correlates with the progressive deterioration of motor functions.

Sod1^{G86R} and Fus$^{\Delta NLS/+}$ mice display altered cortical noradrenergic signalling

To test whether altered neurotransmitter signalling could explain cortical hyperexcitability in *Sod1^{G86R}* and *Fus$^{\Delta NLS/+}$* mice, we conducted liquid chromatography coupled to tandem mass spectrometry (LC-MS) analyses on microdissected motor cortex samples from 45, 60 and 90-day-old *Sod1^{G86R}* and 4-month-old *Fus$^{\Delta NLS/+}$* mice and their age-matched control littermates to measure the concentration of the two main cortical neurotransmitters (glutamate and GABA) and relevant neuromodulators (glycine, serotonin, dopamine, noradrenaline) *(23)*. In *Sod1^{G86R}* mice compared to controls, glutamate was decreased (genotype effect: $p=0.0189$ in two-way ANOVA, **fig. S5, A**). GABA was unchanged (**fig. S5, B**), but glycine was

decreased (genotype effect: p=0.0040 respectively in two-way ANOVA, **fig. S5, C**). Whereas dopamine was unchanged (**fig. S5, D**), serotonin was significantly decreased in *Sod1*^{G86R} animals (genotype effect: p=0.0034 in two-way ANOVA, **Fig. S5, E**), as already reported *(24, 25)*. None of these neurotransmitters and neuromodulators were affected in the *Fus*$^{\Delta NLS/+}$ mice compared to their WT littermates (**fig. S5, F to J**). Noradrenaline (NA) was significantly decreased by 35.24% ± 2.81 in *Sod1*^{G86R} mice (genotype effect, p<0.0001 in two-way ANOVA, **Fig. 5, A**) and by 19.06% ± 2.65 in *Fus*$^{\Delta NLS/+}$ mice (p=0.0019 in two-tailed Student's t-test, **Fig. 5, A**). Similar results were observed in the hippocampus and spinal cord of *Sod1*^{G86R} mice (genotype effect: p<0.0001 in two-way ANOVA for both structures, **fig. S6, A and B**) but not in the spinal cord of *Fus*$^{\Delta NLS/+}$ animals (**fig. S6, C**), pointing to differences in the extent of noradrenergic depletion across regions of the central nervous system and mouse lines. Of note, we observed that animals from the *Fus*$^{\Delta NLS/+}$ mouse line (WT and mutant), displayed on average four times higher NA tissue concentration than animals from the *Sod1*^{G86R} mouse line (WT and mutant), which is likely due to their respective genetic backgrounds (**Fig. 1, A and B)**, as already reported *(44)*.

To further investigate the origins of decreased cortical NA in *Sod1*^{G86R} and *Fus*$^{\Delta NLS/+}$ mice, we labelled and quantified the number of tyrosine hydroxylase (TH)-positive NA neurons in the locus coeruleus (LC) which harbours noradrenergic projection neurons innervating the cerebral cortex and spinal cord (**fig. S7**), and the density of dopamine-beta-hydroxylase (DBH)-positive noradrenergic projections to the motor cortex (**Fig. 5, B and C**). We found an overall significant decrease of TH-positive neurons of 20.93 % ± 3.04 on average in the LC of *Sod1*^{G86R} mice compared to their WT littermates (mixed-effect analysis, genotype effect: p=0.0026, **fig. S7, A and B**). However, paired *post-hoc* comparisons revealed a significant decrease of TH-positive neurons in the LC of *Sod1*^{G86R} mice only at 45 days (p=0.0005 at 45 days, p=0.2114 at 60 days and p=0.0795 at 90 days). In addition, we did not detect any change in soma size (**fig. S7, C**) of TH-positive neurons in the LC of *Sod1*^{G86R} animals. No difference in the number or size of TH-positive neurons was found in the *Fus*$^{\Delta NLS/+}$ animals (**fig. S7, A to C**). However, both mouse lines displayed a significantly decreased density of cortical DBH-positive fibres compared to controls (14.4% ± 2.66, genotype effect: p<0.0001 in mixed-effect analysis for *Sod1*^{G86R} mice; 7.40% ± 1.15, p=0.0289 in two-tailed Student's t-test for *Fus*$^{\Delta NLS/+}$ mice; **Fig. 5, C**), arguing for a more pronounced effect of the *Sod1*^{G86R} and *Fus*$^{\Delta NLS/+}$mutations on noradrenergic axons than on noradrenergic cell bodies. Next, we injected a retrograde adenovirus encoding *GFP* under the human *SYNAPSIN* promoter into the motor cortex of 85-day-old old *Sod1*^{G86R} and WT littermates (**fig. S7, D**), and quantified the number of GFP-positive neurons present in the LC of the animals five days later (**fig. S7, E to G)**. WT and *Sod1*^{G86R} mice displayed comparable amounts of TH- and GFP-positive noradrenergic neurons (**fig. S7, F and G**). Together, the data suggest that, in the *Sod1*^{G86R} and *Fus*$^{\Delta NLS/+}$mouse lines, noradrenergic neurons projecting to the motor cortex may not undergo degeneration, but rather develop with a reduced axonal arborisation and complexity.

To further assess the extent of noradrenergic signalling impairment in ALS mouse models, we ran qPCR and western blot analyses on microdissected motor cortices and performed immunofluorescence experiments to assess the expression of adrenergic receptors and NA degradation enzymes (**Fig. 5, D to O,** and **fig. S8**). Expression of Beta 1 (**fig. S8, A**) and Alpha 2C (**fig. S8, B**) adrenergic receptor genes was unaltered in both mouse lines. Contrastingly, Alpha2A and Alpha2B adrenergic receptor mRNA expression was decreased in the motor cortex of *Sod1*^{G86R} mice compared to WT (genotype effect in mixed-effect analysis: p=0.0002 for *Adra2a*, p<0.0001 for *Adra2b*, **Fig. 5, D and E**), and of *Fus*$^{\Delta NLS/+}$ mice compared to WT (p=0.0112 for *Adra2a*, and p=0.0042 for *Adra2b* in two-sided t-test; **Fig. 5, D and E**). Beta 2 adrenergic receptor gene expression was also decreased in *Sod1*^{G86R} (p=0.0038), but unchanged in *Fus*$^{\Delta NLS/+}$ mice compared to their respective WT littermates (**Fig. 5, F**). Western blot analyses revealed decreased protein expression of Alpha 2B and Beta 2 adrenoreceptors in *Fus*$^{\Delta NLS/+}$ mice (p=0.0336 for Alpha 2B and p=0.0152 for Beta 2, **Fig. 5, H and I** and **S8, D and E**), but not in *Sod1*^{G86R} mice. Immunofluorescence further allowed us to reveal and quantify the expression of these receptors in neuronal subpopulations of interest within cortical layer V, namely, CTIP2-positive excitatory neurons, parvalbumin- (PV-) and somatostatin- (SST-) positive interneurons (**Fig. 5, J to L** and **fig. S8, F and G**). Alpha 2A, was overall found enriched in CTIP2-positive compared to PV- and SST-positive neurons, and its protein expression was significantly decreased in CTIP2-positive neurons of 60-day-old *Sod1*^{G86R} mice compared to their WT littermates (p=0.0004 in multiple comparison test; **Fig. 5, J**). Alpha 2B and Alpha 2C were found enriched in CTIP2- and SST-positive neurons compared to PV-positive neurons but their expression by these neuronal subpopulations was not affected in *Sod1*^{G86R} animals (**Fig. 5, J** and **fig. S8, F**). Noradrenergic impairment was further indicated by the differential expression of genes encoding NA degradation enzymes: monoamine oxidases A and B and catechol-O-methyltransferase (*Maoa*, *Maob*, *Comt*). *Maoa* expression was unchanged (**fig. S8, G**), *Maob* expression was significantly increased in *Sod1*^{G86R} animals (genotype effect: p=0.0106 in mixed-effect analysis) but not in *Fus*$^{\Delta NLS/+}$ animals (p=0.5319 in two-sided t-test; **fig. S8, H**), and *Comt* expression was unaffected in *Sod1*^{G86R} animals (genotype effect: p=0.2094 in mixed-effect analysis) but significantly increased in *Fus*$^{\Delta NLS/+}$ animals (p=0.0131 in two-sided t-test, **fig. S8, I**), suggesting different regulatory mechanisms affecting each gene in each mouse line. Together, the data indicate that noradrenergic signalling is impaired in the motor cortex of both *Sod1*^{G86R} and *Fus*$^{\Delta NLS/+}$ mouse models of ALS, reflected in decreased NA concentration, decreased noradrenergic innervation and altered expression of noradrenergic receptors and degradation enzymes.

Behaving *SOD1*^{G93A} and *Fus*$^{\Delta NLS/+}$ mice display compromised NA release in the primary motor cortex

We next asked whether NA release was also affected in vivo. As the activity of corticopetal axonal NA projections strongly correlates with locomotion *(45, 46)*, we probed running-associated NA release by

means of in vivo two-photon imaging in a third ALS mouse model, the *SOD1*^{G93A} mice, as well as in *Fus*$^{\Delta NLS/+}$*mice* and their respective WT littermates, while animals were head-fixed moving on a spherical treadmill (**Fig. 6, A** and **fig. S9**). Expression of the genetically encoded NA indicator GRABNE1m was achieved through AAV transduction. We observed a clear increase in fluorescence, corresponding to NA release, associated with running onsets in the primary motor cortex layer II/III (**Fig. 6, B and C** and **fig. S9, A to C**). When comparing the locomotion-associated signal in early symptomatic *SOD1*^{G93A} (90 day-old) and *Fus*$^{\Delta NLS/+}$mice (4 months old) mice with WT controls, we found a strong reduction within -0.5 to +1.5 s of running onset (11.18 ± 2.83 in WT vs -0.95 ± 2.42 *SOD1*^{G93A}, p=0.0023, **Fig. 6, D;** 9.88 ± 3.25 in WT vs -4.53 ± 2.58 *Fus*$^{\Delta NLS/+}$, p=0.0084, Wilcoxon rank sum test for the area under the curve from -0.5 to 1.5s with respect to locomotion onset, **fig. S9, D**), illustrating a strong reduction of NA release. To rule out the contribution of running velocities, we computed the tuning curves of this response, by measuring the fluorescence intensity change as a function of average running speed within a 3s-window after running onset. The tuning curve revealed a positive linear relationship of fluorescence intensity and running velocity in WT mice (y=0.48x + 0.01, R^2=0.91, slope p=0.012, **Fig. 6, E**). In *SOD1*^{G93A} mice, however, there was not only a strong overall reduction in locomotion-associated NA release, but moreover, the velocity-dependent increase in fluorescence was greatly diminished (y=0.13x + 0.003, R^2=0.482, slope p=0.19, difference in slope difference between WT and *SOD1*^{G93A} p=0.0148, **Fig. 6, E**). A similar reduction was found in *Fus*$^{\Delta NLS/+}$ mice (linear fit of the maximum values within -0.5 to 1.5s of the running onset in the different velocity bins in WT: y=0.638x + 0.004, R^2=0.862 and *Fus*$^{\Delta NLS/+}$ mice: y=0.219x + 0.005, R^2=0.313, intercept difference between WT and *Fus*$^{\Delta NLS/+}$ p=0.0462, one-way ANOVA, **fig. S9, E**). As NA release could potentially also occur with a temporal offset within a given brain area, we also assessed the synchrony of NA release within a given field of view by computing the pairwise correlation coefficient between individual regions of interest (**Fig. 6, F**). This analysis revealed no significant difference between WT and *SOD1*^{G93A} mice (p=0.64, **Fig. 6, G**). Together, our data show that NA release is strongly impaired in M1 of *SOD1*^{G93A} and *Fus*$^{\Delta NLS/+}$ mice.

Sporadic ALS patients present with altered cortical noradrenergic signalling

To assess the relevance of our findings in ALS patients, we conducted LC-MS analyses on post-mortem motor cortex, LC and spinal cord from sporadic patients and controls (**Table S1),** and performed transcriptomic analyses on post-mortem motor and prefrontal cortices from sporadic patients and controls. LC-MS analyses revealed a significant decrease of NA in the motor cortex and LC of patients compared to healthy controls (p=0.039 and p=0.01 respectively, **Fig. 7, A**), but not in the spinal cord (**Fig. 7, A**). NA concentrations in post-mortem samples did not correlate with the age of death, neither amongst the control nor amongst the samples from patients (Pearson correlation, p=0.4409, R^2=0.1228 for controls and

p=0.7306, R^2=0.01803 for patients, **Fig. 7, B** and **Table S1**). Glutamate concentrations were unaltered in the motor cortex and spinal cord, but significantly decreased in the LC of ALS patients compared to controls (p=0.003, **fig. S10, A**). GABA concentrations were significantly decreased in the motor cortex and LC of patients compared to healthy individuals (p=0.034 and 0.0095 respectively, **fig. S10, B)**. Finally, as expected, serotonin concentrations were decreased in the motor cortex of patients compared to controls (p=0.0078, **Fig. S10, C**), but were not significantly altered in the spinal cord of patients. Thus, the LC-MS data indicate that ALS patients present with decreased NA in the motor cortex and LC, along with decreased GABA in these same structures and decreased glutamate in the LC, suggesting multifaceted alterations of proper circuit function within these brain regions. Transcriptomic analyses revealed significantly decreased expression of *ADRA1B* (FDR=0.0020), *ADRA1D*, (FDR=0.00638), *ADRB1* (FDR=0.00014) and *ADRA2B* (FDR=0.00010; **Fig. 7, C**). Together, LC-MS and transcriptomic data indicate that noradrenergic homeostasis is also alerted in the motor cortex of sporadic patients.

Experimental modulation of noradrenergic homeostasis alters cortical circuit function in WT and $Sod1^{G86R}$ mice

To test whether impaired NA homeostasis could contribute to cortical hyperexcitability and broader network dysfunction, we first experimentally triggered cortical NA depletion in WT mice, taking advantage of the N-(2-chloroethyl)-N-ethyl-2-bromobenzylamine (DSP-4) neurotoxin that selectively affects noradrenergic neurons of the LC *(47)* (**Fig. 8, A to E** and **fig. S11**). As expected, DSP-4 treatment selectively decreased cortical NA (p<0.0001, **fig. S11, A**) without affecting the amounts of glutamate, GABA, serotonin and dopamine (**fig. S11, A**). A first cohort of wild type mice underwent PTZ susceptibility test, prior to and 8 days after DSP-4 injection (**Fig. 8, A**). DSP-4 treatment significantly increased PTZ susceptibility by 62.03% ±8.26 in these mice (p=0.0005, **Fig. 8, B and C**). A second cohort of wildtype mice underwent T-HG PAC measurements during REM sleep, prior to and 48 hours after DSP-4 injection (**Fig. 8, D**). T-HG PAC was significantly decreased in mice upon DSP-4 administration compared to the pre-treatment condition (p=0.0048, **Fig. 8, E**), although theta, high gamma and total power remained unchanged (**fig. S11, B to D**). DSP-4 administration also induced decreased T-LG PAC during REM sleep (p=0.0098, **fig. S11, F**) that might arise partly from overall decreased low gamma power (p=0.0282, **fig. S11, E**). Together, the data indicate that experimentally induced cortical NA depletion is sufficient to trigger cortical hyperexcitability as manifested by increased PTZ susceptibility and decreased T-HG PAC. This phenotype is reminiscent of that observed in the $Sod1^{G86R}$ and $Fus^{\Delta NLS/+}$ mouse models of ALS.

Second, we tested whether experimental supplementation of NA in $Sod1^{G86R}$ mice would be sufficient to revert cortical hyperexcitability (**Fig. 8, F and G)**. We used a combination of L-threo 3,4-dihydroxyphenylserine (L-DOPS), and benserazide. L-DOPS is a synthetic precursor of NA that is

metabolized to NA by the aromatic acid decarboxylases. Benserazide is an inhibitor of the aromatic acid decarboxylases that does not cross the blood brain barrier. Thus, the combination of L-DOPS and benserazide allows to increase NA concentration selectively in the central nervous system *(48)*. We failed to detect a significant increase of NA in L-DOPS + Benserazide-treated animals, compared to saline-injected animals, all harvested 12 hours post-injection, independent of their genotype (**fig. S12, A**), which likely arises from the very short effect of L-DOPS on NA concentration in the central nervous system that peaks 5 hours post-injection *(48)*. Glutamate, GABA and serotonin remained unaffected (**fig. S12, B to D**). T-HG PAC was significantly increased in *Sod1*^{G86R} animals (p=0.0290 for *Sod1*^{G86R}, **Fig. 8, G**), without any significant effect on theta, high gamma and total powers (**fig. S12, E to G**). L-DOPS + benserazide injection had no effect on the T-HG PAC in WT animals (**Fig. 8, G**), but significantly increased both theta and total powers in these animals (p=0.0060 and p=0.0039 respectively, **Fig. S12, E and G**).

To finally test whether cortical hyperexcitability could be reduced over a longer period of time, we selected yohimbine, an Alpha 2 antagonist described to increase synaptic NA concentration by blocking pre-synaptic Alpha 2A adrenoreceptors that are responsible for the negative feedback on noradrenergic release *(49)*. Chronic in vivo two-photon imaging in 4-month-old *Fus*$^{\Delta NLS/+}$mice and their WT littermates revealed a significant increase in NA release after 10 days of yohimbine treatment (6 mg/kg/day) in WT control, and to a lesser degree also in *Fus*$^{\Delta NLS/+}$mice (fold change in WT: Baseline *vs* day 10, 1.14 + [1.04 1.24], p=0.0027 ; day 2 *vs* day 10 p=0.0047; *Fus*$^{\Delta NLS/+}$: Baseline *vs* day 10, 1.19 + [0.97 1.29], data are median + 95% CI, p=0.022, day 2 *vs* day 10, p=0.092, all Wilcoxon rank sum tests, **fig. S13, A to F**). Chronic imaging in saline-treated mice instead did not reveal any increase of the fluorescent signal (**fig. S13, G**). T-HG PAC was then assessed in WT and *Sod1*^{G86R} mice during REM sleep, prior (45 days) to and every 10 days upon daily injection of yohimbine (**Fig. 8, H**). Yohimbine significantly increased T-HG PAC in *Sod1*^{G86R} mice during at least 20 days (p=0.0195 and p=0.0052 between baseline and 10 and 20 days-post treatment respectively, in mixed-effects analysis followed by multiple comparisons test, **Fig. 8, I**), meaning, until at least 65 days of age. Finally, we tested the consequences a chronic yohimbine treatment, initiated at the age of 60 days, has on disease onset, motor phenotype and survival in *Sod1*^{G86R} mice (**fig. S14**). The results indicate that the treatment did neither modify the onset, nor survival or symptoms severity (**fig. S14**). This lack of efficiency may be attributed to the temporally limited effect of yohimbine on cortical hyperexcitability.

Together, these experiments indicate that impaired cortical NA homeostasis contributes to cortical hyperexcitability and motor cortex network dysfunction in ALS. Follow-up studies will be needed to identify a drug or method to permanently correct NA impairment and cortical hyperexcitability in mice prior to assessing the consequences on symptom onset, progression and survival.

DISCUSSION

Cortical hyperexcitability has been so far detected in ALS patients using paired-pulse TMS protocols *(5)*. The method, however, falls short in cases of advanced UMN and LMN dysfunction and degeneration that prevents faithful measurements at the level of the muscles. We thus sought to provide proof of principle experiments that cortical hyperexcitability can be assessed by means of non-invasive EEG measurements, independent of the integrity of the corticospinal pathway and neuro-muscular connectivity.

We reasoned that cortical circuit excitation/inhibition (E/I) imbalance could be approached in rodents by combining ECoG with other established means, such as the sensitivity to the $GABA_A$ antagonist PTZ *(32)* and theta-gamma PAC *(11, 12)*. Compared to their respective WT littermates, $Sod1^{G86R}$ and $Fus^{\Delta NLS/+}$ displayed increased sensitivity to PTZ, indicative of a hyperexcitable network. The underlying molecular and cellular mechanisms of which might, however, be manifold, including dysfunction of GABAergic inhibitory neurons as well as enhanced excitability of pyramidal neurons *(6, 7)*. PTZ is commonly used to probe for an epileptic phenotype in models of CNS disorders, including AD *(33)*, as about 10% of AD cases display epileptic discharges or seizures *(50)*. To the best of our knowledge, such a comorbidity has never been described in ALS, and no common genetic risk has been reported *(51)*. Accordingly, neither $Sod1^{G86R}$ nor $Fus^{\Delta NLS/+}$ animals displayed any convulsive seizures upon the application of 30mg/kg of PTZ, a dose which otherwise readily triggers epileptic seizures in animal models of tauopathy or FTD *(52, 53)*. Thus, our results suggest that $Sod1^{G86R}$ and $Fus^{\Delta NLS/+}$ mice recapitulate cortical hyperexcitability.

Cortical E/I imbalance can further be assessed in vivo by EEG/ECoG recordings combined with PAC analyses. PAC has been reported both in human and rodent brains, between different slow and fast frequency bands, and is modulated in a task- and disease-dependent manner *(54)*. Studies conducted in the motor cortex of rats and humans indicate strong theta-gamma coupling in this area *(38-40)*. In addition, EEG recordings in chronic hemiparetic stroke patients demonstrated that theta-gamma coupling was increased during brain-computer interface rehabilitation therapy *(39)*. Importantly, the effect was selectively observed in the C_3 and C_4 channels, and selective to theta-gamma PAC (as opposed to alpha-gamma and beta-gamma) *(39)*. All these data prompted us to assess theta-gamma PAC in ALS mouse models and patients over the sensory-motor areas. We report here that two mouse models of ALS and FTD, $Sod1^{G86R}$ and $Fus^{\Delta NLS/+}$ mice, present with decreased theta-gamma PAC, already during presymptomatic stages and throughout their entire life time. Together with their increased susceptibility to PTZ, our data

suggest that preclinical models of the disease display cortical dysfunction reminiscent of cortical hyperexcitability. These findings are of translational relevance, since we also found decreased theta-gamma PAC in ALS patients. Compromised PAC was not due to changes in absolute power, as described in late-stage ALS, when patients enter a locked-in state *(55, 56)*. Of note, we found more pronounced changes in PAC during REM sleep compared to wakefulness in the two mouse models of the disease. In ALS patients, however, the detection of REM sleep episodes is hampered by progressive paralysis affecting also eye movements *(55)*, which complicates this assessment. We thus opted to perform EEG recordings in awake patients. Decreased theta-gamma PAC was most prominently detected over the left motor area, which could be explained by the fact that most of our participants were right-handed. Investigations of larger cohorts, including left-handed participants, will however be needed to address this aspect in more detail. Decreased theta-gamma PAC did not correlate with UMN impairment, indicating its potential to reveal cortical network dysfunction independent of UMN damage, noticeably heterogeneous across patients *(1)*. Decreased theta-gamma PAC correlated instead with disease progression, strongly encouraging future studies in familial ALS patients and presymptomatic mutation carriers in order to determine whether it has the potential to become an indicator of early cortical impairment and disease stage in ALS, potentially improving diagnosis and prognosis.

Taking advantage of comparable theta-gamma PAC impairment in sporadic ALS patients and mouse models, we strove to gain insight into its cellular and molecular mechanisms. We reasoned that altered E/I balance could at least in part rely on neuromodulatory alterations *(23, 57)*. We observed a mild decrease of glutamate in the motor cortex of *Sod1*^{G86R} mice, but not in that of *Fus*$^{\Delta NLS/+}$ mice nor ALS patients. GABA was unaltered in the motor cortex of the two mouse models but decreased in patients, which could reflect a greater impairment of the cortical GABAergic system in ALS patients compared to mouse models. We further confirmed a decrease of serotonin in the motor cortex of ALS patients and *Sod1*^{G86R} mice, in agreement with previous studies *(24, 25)*. Most critically, we provide evidence of decreased concentration of NA in the motor cortex of sporadic ALS patients, which was conserved in the *Sod1*^{G86R}, *Fus*$^{\Delta NLS/+}$ and *SOD1*^{G93A} mouse models of the disease. Decreased NA concentration was also observed in the LC of ALS patients, but not in spinal cord. In the LC of ALS patients, we also found decreased glutamate and GABA that may reflect a global functional impairment of this nucleus and could potentially also underlie the noradrenergic deficits observed in both the LC itself and the motor cortex of patients. Former HPLC studies conducted on spinal cord homogenates from ALS patients revealed either decreased *(58)* or instead increased *(59)* concentration of NA. In the CSF of ALS patients, however, NA was found increased *(60-62)*, which may reflect a dysfunction of the central noradrenergic system. Decreased NA concentration have so far been mostly reported in AD and PD, in which cases it was linked to an early degeneration of

the LC *(27, 28)*. Whereas histological defects, such as neuronal loss and neurofibrillary tangles, were observed in the LC of ALS patients *(63, 64)*, typical pTDP-43 pathology was strikingly absent *(65)*. This, however, does not *per se* rule out an impairment of noradrenergic neurons. Quantification of TH-positive neurons in the LC of *Sod1*^{G86R}, *Fus*$^{\Delta NLS/+}$, along with retrograde labelling of LC neurons projecting to the motor cortex in *Sod1*^{G86R} mice, excluded the hypothesis of major noradrenergic neuron degeneration in these animals. Instead, the decreased noradrenergic fibre density in the motor cortex of *Sod1*^{G86R} and *Fus*$^{\Delta NLS/+}$ mice, along with the increased expression of *Maob* and *Comt* in *Sod1*^{G86R} and *Fus*$^{\Delta NLS/+}$ mice respectively, are likely to contribute to NA deficiency in this region. One can speculate that decreased NA fibre density or altered LC function may similarly contribute to decreased NA release seen in behaving *SOD1*^{G93A} and *Fus*$^{\Delta NLS/+}$ animals. NA release is strongly associated with wakefulness, and NA neurons of the LC are virtually silent during REM sleep, a phenomenon that is at least partly attributed to the strong control of the suprachiasmatic nucleus, the central pacemaker of the circadian timing system, over the LC (reviewed in *(66)*). It is thus tempting to speculate that NA release during wakefulness, even if diminished in ALS, may partially dampen the otherwise observed cortical hyperexcitability, and that the absence of NA during REM sleep would further potentiate cortical hyperexcitability. This might explain why theta-gamma PAC deficits are more prominent during REM sleep than during active wakefulness in ALS mouse models. In sum, the mechanisms driving the dysfunction or degeneration of NA neurons in the LC as well as reduced NA innervation and release in cortical areas of ALS patients and mouse models warrant further scrutiny.

Previous reports have also shown that NA decreases excitation by lowering AMPA-mediated glutamatergic transmission through Alpha1 and Alpha2 adrenoreceptors, and increases the synaptic responses mediated by $GABA_A$ receptors *(67)*. Accordingly, LC stimulation was demonstrated to protect epileptic patients from seizures *(68-70)*. In addition, both pharmacologically and genetically induced NA deficiency was demonstrated to increase CNS excitability in mice, with increased susceptibility to various convulsant agents, and increased c-Fos expression in the neocortex, hippocampus and amygdala *(71, 72)*. In line with these reports, we also found an increase in cortical excitability assessed upon PTZ challenge, as well as a decrease in theta-gamma PAC in WT mice treated with DSP-4. Overall, these studies indicate that NA can exert a global inhibitory effect on cortical activity, and support the notion that NA deficiency contributes to cortical hyperexcitability in ALS. Importantly, we also show that both NA supplementation and Alpha2 blockage in *Sod1*^{G86R} mice can rescue the PAC deficit at least transiently. These data indicate that NA deficiency contributes to cortical activity dysregulation, and that increasing cortical NA can help restore it. We attempted to chronically restore NA signalling using yohimbine, which, however, only exerted a transient effect on cortical excitability that might explain the absence of beneficial effect on

disease onset and progression. Additional strategies to maintain NA homeostasis in a more sustained manner will be needed to address this important question. It is noteworthy that numerous drugs exist that increase central NA with indications for attention deficit disorder, narcolepsy and excessive sleepiness, such as amphetamines, atomoxetine, methylphenidate or solriamfetol *(73)*, or anxiety and depression, such as serotonin and noradrenaline reuptake inhibitors (SNRIs), antagonists of inhibitory presynaptic serotonin and noradrenaline receptors, or inhibition of the monoamine oxidase *(74)*. These represent many possible candidates to restore central NA homeostasis in ALS mouse models and assess the consequences on disease onset and progression. Notably, the risk of depression is increased in ALS patients *(75)*, in which case antidepressants can be prescribed. However, with the exception of rasagiline *(76)*, a MAO-B inhibitor, such drugs have, to our knowledge, never been directly assessed for their ability to slow down disease progression in ALS patients. Apart from their effect on the CNS, it is worth mentioning that guanabenz, an Alpha2 agonist, and clenbuterol, a Beta2 agonist, have been tested in ALS patients for their ability to prevent misfolded protein accumulation, or to protect muscle mass and strength, respectively, and provided encouraging first results *(77, 78)*. Investigating the effect of these drugs on cortical excitability would be of particular interest in the context of our results.

There are some limitations to our study including the methodology we have employed to assess PAC in rsEGG, which was done over a period of 5 minutes. Given that PAC is not homogeneous over time, longer recording times or further segmentation of the recordings time may in the future reduce the variability of the MI and unravel even more pronounced and robust PAC deficits in patients. In addition, although patients' MI negatively correlated with disease progression, it is noteworthy that the progression rate was calculated from a single ALSFRS-r measurement. Future studies will be needed to include several EEG recordings and corresponding ALSFRS-r assessments to better evaluate how PAC deficits reflect disease progression. Another limitation lies in human NA measurements that were performed on postmortem tissues and not from the same individuals that underwent EEG recording. Therefore, correlation between NA deficits and PAC impairment was not possible, and future studies will be needed to address this limitation potentially through longitudinal NA measurements in the CSF.

Taken together, we here show that compromised theta-gamma PAC is present in ALS patients and mouse models of the disease and reflects cortical hyperexcitability, which in turn is at least in part driven by NA deficiency. Although the exact mechanisms, through which NA alterations contribute to cortical hyperexcitability remain to be determined, the central noradrenegric system offers a promising new pathway to modulate cortical network dysfunction in ALS.

MATERIALS AND METHODS

Study design

The aims of this study were (i) to test whether cortical hyperexcitability in mouse models and patients with ALS could manifest in EEG and ECoG as altered theta-gamma coupling, and (ii) to gain insight into its cellular and molecular origins. ECoG in the *Sod1*^{G86R} and *Fus*$^{\Delta NLS/+}$ ALS mouse models was performed and theta-gamma phase-amplitude-coupling (PAC) characterized and compared to healthy control mice. Sample size was estimated based on former studies in rodents (*17*). In vivo two-photon imaging in behaving mice, liquid-chromatography-mass spectrometry, histology and transcriptomics were used to characterize changes in NA signalling in ALS mouse models. Sample size was estimated based on former studies (*20*). All mouse experiments were approved by the local ethics committee of Strasbourg University (CREMEAS, APAFIS#12138-2017111016579993 v3) and the government of Upper Bavaria. Experiments on presymptomatic animals were blinded. EEG data from 26 patients with ALS and 26 matched healthy controls was obtained. EEG procedures conformed to the lasted revision of the Code of Ethics of the World Medical Association (Declaration of Helsinki) and were approved by the ethics committee of INSERM (protocol C17-70) and by the national ethical authorities (CPP Ouest II Angers, n° 18.07.11.57804 2018/58; RCB 2018), and recorded in public register (Clinical.Trials.gov, NCT03694132). Each participant provided their written informed consent. The PAC analysis in patients is part of a more extensive study primarily focused on investigating the integration of sensory feedback at the cerebral level in ALS, suing EEG, MEG and MRI. Using a 5% alpha risk, we determined a sample size for a t-test and its corresponding power. The statistical analysis yielded a projected sample size of 26 subjects, with a test power of 75%. Recordings on humans were not blinded due to the motor phenotypes of ALS patients. LC-MS on post-mortem tissue samples from 9 patients with sporadic ALS and 7 healthy controls, and transcriptomics on post-mortem tissue motor and frontal cortices from 27 ALS patients and 29 healthy controls were applied to quantify disease related changes in CNS NA. Sample size was based on availability of tissue samples and transcriptomic data. Patients or families had provided written informed consent.

List of Supplementary Materials

Materials and Methods

fig. S1 to S14

Table S1

Data File S1

References and Notes

1. J. M. Shefner, A. Al-Chalabi, M. R. Baker, L.-Y. Cui, M. de Carvalho, A. Eisen, J. Grosskreutz, O. Hardiman, R. Henderson, J. M. Matamala, H. Mitsumoto, W. Paulus, N. Simon, M. Swash, K. Talbot, M. R. Turner, Y. Ugawa, L. H. van den Berg, R. Verdugo, S. Vucic, R. Kaji, D. Burke, M. C. Kiernan, A proposal for new diagnostic criteria for ALS, *Clin Neurophysiol* **131**, 1975–1978 (2020).

2. S. A. Goutman, O. Hardiman, A. Al-Chalabi, A. Chiò, M. G. Savelieff, M. C. Kiernan, E. L. Feldman, Emerging insights into the complex genetics and pathophysiology of amyotrophic lateral sclerosis, *The Lancet Neurology* **21**, 465–479 (2022).

3. N. Geevasinga, P. Menon, P. H. Özdinler, M. C. Kiernan, S. Vucic, Pathophysiological and diagnostic implications of cortical dysfunction in ALS, *Nat. Rev. Neurol.*, 1–11 (2016).

4. S. Vucic, G. A. Nicholson, M. C. Kiernan, Cortical hyperexcitability may precede the onset of familial amyotrophic lateral sclerosis, *Brain : a journal of neurology* **131**, 1540–1550 (2008).

5. S. Agarwal, G. Koch, A. E. Hillis, W. Huynh, N. S. Ward, S. Vucic, M. C. Kiernan, Interrogating cortical function with transcranial magnetic stimulation: insights from neurodegenerative disease and stroke, *Journal of Neurology, Neurosurgery & Psychiatry* **90**, 47–57 (2019).

6. A. Brunet, G. Stuart-Lopez, T. Burg, J. Scekic-Zahirovic, C. Rouaux, Cortical Circuit Dysfunction as a Potential Driver of Amyotrophic Lateral Sclerosis, *Front Neurosci* **14** (2020).

7. Z. I. Gunes, V. W. Y. Kan, X. Q. Ye, S. Liebscher, Exciting Complexity: The Role of Motor Circuit Elements in ALS Pathophysiology, *Front Neurosci* **14**, 1–30 (2020).

8. C. S. Khademullah, A. J. Aqrabawi, K. M. Place, Z. Dargaei, X. Liang, J. C. Pressey, S. Bedard, J. W. Yang, D. Garand, I. Keramidis, A. Gasecka, D. Côté, Y. De Koninck, J. Keith, L. Zinman, J. Robertson, J. C. Kim, M. A. Woodin, Cortical interneuron-mediated inhibition delays the onset of amyotrophic lateral sclerosis, *Brain : a journal of neurology* **143**, 800–810 (2020).

9. L. A. Reale, M. S. Dyer, S. E. Perry, K. M. Young, T. C. Dickson, A. Woodhouse, C. A. Blizzard, Pathologically mislocalised TDP-43 in upper motor neurons causes a die-forward spread of ALS-like pathogenic changes throughout the mouse corticomotor system, *Progress in Neurobiology* **226**, 102449 (2023).

10. R. T. Canolty, E. Edwards, S. S. Dalal, M. Soltani, S. S. Nagarajan, H. E. Kirsch, M. S. Berger, N. M. Barbaro, R. T. Knight, High Gamma Power Is Phase-Locked to Theta Oscillations in Human Neocortex, *Science* **313**, 1626–1628 (2006).

11. G. Buzsáki, X.-J. Wang, Mechanisms of Gamma Oscillations, *Annu. Rev. Neurosci.* **35**, 203–225 (2012).

12. S. Keeley, A. A. Fenton, J. Rinzel, Modeling fast and slow gamma oscillations with interneurons of different subtype, *Journal of Neurophysiology* **117**, 950–965 (2017).

13. C. de Hemptinne, E. S. Ryapolova-Webb, E. L. Air, P. A. Garcia, K. J. Miller, J. G. Ojemann, J. L. Ostrem, N. B. Galifianakis, P. A. Starr, Exaggerated phase-amplitude coupling in the primary motor cortex in Parkinson disease, *Proceedings of the National Academy of Sciences* **110**, 4780–4785 (2013).

14. A. Devergnas, M. Caiola, D. Pittard, T. Wichmann, Cortical Phase-Amplitude Coupling in a Progressive Model of Parkinsonism in Nonhuman Primates, *Cerebral Cortex* **29**, 167–177 (2019).

15. A. Ahnaou, D. Moechars, L. Raeymaekers, R. Biermans, N. V. Manyakov, A. Bottelbergs, C. Wintmolders, K. Kolen, T. Casteele, J. A. Kemp, W. H. Drinkenburg, Emergence of early alterations in network oscillations and functional connectivity in a tau seeding mouse model of Alzheimer's disease pathology, *Scientific Reports*, 1–14 (2017).

16. M. S. Goodman, S. Kumar, R. Zomorrodi, Z. Ghazala, A. S. M. Cheam, M. S. Barr, Z. J. Daskalakis, D. M. Blumberger, C. Fischer, A. Flint, L. Mah, N. Herrmann, C. R. Bowie, B. H. Mulsant, T. K. Rajji, Theta-Gamma Coupling and Working Memory in Alzheimer's Dementia and Mild Cognitive Impairment, *Frontiers in Aging Neuroscience* **10**, 101 (2018).

17. R. Goutagny, N. Gu, C. Cavanagh, J. Jackson, J.-G. Chabot, R. Quirion, S. Krantic, S. Williams, Alterations in hippocampal network oscillations and theta-gamma coupling arise before Aβ overproduction in a mouse model of Alzheimer's disease, *European Journal of Neuroscience* **37**, 1896–1902 (2013).

18. C. S. Musaeus, Electroencephalographic Cross-Frequency Coupling as a Sign of Disease Progression in Patients With Mild Cognitive Impairment: A Pilot Study, *Frontiers in Neuroscience*, 1–10 (2020).

19. L. E. Hughes, T. Rittman, T. W. Robbins, J. B. Rowe, Reorganization of cortical oscillatory dynamics underlying disinhibition in frontotemporal dementia, *Brain : a journal of neurology* **141**, 2486–2499 (2018).

20. J. Scekic-Zahirovic, I. Sanjuan-Ruiz, V. Kan, S. Megat, P. Rossi, S. Dieterlé, R. Cassel, M. Jamet, P. Kessler, D. Wiesner, L. Tzeplaeff, V. Demais, S. Sahadevan, K. M. Hembach, H.-P. Müller, G. Picchiarelli, N. Mishra, S. Antonucci, S. Dirrig-Grosch, J. Kassubek, V. Rasche, A. Ludolph, A.-L. Boutillier, F. Roselli, M. Polymenidou, C. Lagier-Tourenne, S. Liebscher, L. Dupuis, Cytoplasmic FUS triggers early behavioral alterations linked to cortical neuronal hyperactivity and inhibitory synaptic defects, *Nature Communications* **12**, 1–19 (2021).

21. K. A. Guttenplan, M. K. Weigel, D. I. Adler, J. Couthouis, S. A. Liddelow, A. D. Gitler, Ben A Barres, Knockout of reactive astrocyte activating factors slows disease progression in an ALS mouse model, *Nature Communications* **11**, 1–9 (2020).

22. P. J. Magistretti, I. Allaman, Lactate in the brain: from metabolic end-product to signalling molecule, *Nat. Rev. Neurosci.* **19**, 235–249 (2018).

23. C. Vitrac, M. Benoit-Marand, Monoaminergic Modulation of Motor Cortex Function, *Frontiers in Neural Circuits* **11**, 2195 (2017).

24. C. Dentel, L. Palamiuc, A. Henriques, B. Lannes, O. Spreux-Varoquaux, L. Gutknecht, F. Rene, A. Echaniz-Laguna, J.-L. Gonzalez de Aguilar, K. P. Lesch, V. Meininger, J.-P. Loeffler, L. Dupuis,

Degeneration of serotonergic neurons in amyotrophic lateral sclerosis: a link to spasticity, *Brain : a journal of neurology* **136**, 483–493 (2013).

25. H. El Oussini, J. Scekic-Zahirovic, P. Vercruysse, C. Marques, S. Dirrig-Grosch, S. Dieterlé, G. Picchiarelli, J. Sinniger, C. Rouaux, L. Dupuis, Degeneration of serotonin neurons triggers spasticity in amyotrophic lateral sclerosis, *Ann Neurol.* **82**, 444–456 (2017).

26. J. Lotharius, P. Brundin, Pathogenesis of Parkinson's disease: dopamine, vesicles and alpha-synuclein, *Nat. Rev. Neurosci.* **3**, 932–942 (2002).

27. N. Holland, T. W. Robbins, J. B. Rowe, The role of noradrenaline in cognition and cognitive disorders, *Brain : a journal of neurology* **144**, 2243–2256 (2021).

28. A. C. Peterson, C.-S. R. Li, Noradrenergic Dysfunction in Alzheimer"s and Parkinson"s Diseases-An Overview of Imaging Studies, *Frontiers in Aging Neuroscience* **10**, 127 (2018).

29. M. E. Ripps, G. W. Huntley, P. R. Hof, J. H. Morrison, J. W. Gordon, Transgenic mice expressing an altered murine superoxide dismutase gene provide an animal model of amyotrophic lateral sclerosis, *Proc. Natl. Acad. Sci. U.S.A.* **92**, 689–693 (1995).

30. J. Scekic-Zahirovic, H. El Oussini, S. Mersmann, K. Drenner, M. Wagner, Y. Sun, K. Allmeroth, S. Dieterlé, J. Sinniger, S. Dirrig-Grosch, F. Rene, D. Dormann, C. Haass, A. C. Ludolph, C. Lagier-Tourenne, E. Storkebaum, L. Dupuis, Motor neuron intrinsic and extrinsic mechanisms contribute to the pathogenesis of FUS-associated amyotrophic lateral sclerosis, *Acta Neuropathol.* **133**, 887–906 (2017).

31. C. Marques, T. Burg, J. Scekic-Zahirovic, M. Fischer, C. Rouaux, Upper and Lower Motor Neuron Degenerations Are Somatotopically Related and Temporally Ordered in the Sod1 Mouse Model of Amyotrophic Lateral Sclerosis, *Brain Sciences* **11**, 1–18 (2021).

32. J. Van Erum, D. Van Dam, P. P. De Deyn, PTZ-induced seizures in mice require a revised Racine scale, *Epilepsy & Behavior* **95**, 51–55 (2019).

33. S. Maeda, B. Djukic, P. Taneja, G.-Q. Yu, I. Lo, A. Davis, R. Craft, W. Guo, X. Wang, D. Kim, R. Ponnusamy, T. M. Gill, E. Masliah, L. Mucke, Expression of A152T human tau causes age- dependent neuronal dysfunction and loss in transgenic mice, *EMBO Rep* **17**, 530–551 (2016).

34. N. A. Copping, A. Adhikari, S. P. Petkova, J. L. Silverman, Genetic backgrounds have unique seizure response profiles and behavioral outcomes following convulsant administration, *Epilepsy & Behavior* **101**, 106547 (2019).

35. R. A. Kohnken, D. J. Schwahn, Lack of Chronic Histologic Lesions Supportive of Sublethal Spontaneous Seizures in FVB/N Mice, *Comp Med* **66**, 105–111 (2016).

36. H. M. Chameh, S. Rich, L. Wang, F.-D. Chen, L. Zhang, P. L. Carlen, S. J. Tripathy, T. A. Valiante, Diversity amongst human cortical pyramidal neurons revealed via their sag currents and frequency preferences, *Nature Communications* **12**, 1–15 (2021).

37. C. M. Florez, R. J. McGinn, V. Lukankin, I. Marwa, S. Sugumar, J. Dian, L. N. Hazrati, P. L. Carlen, L. Zhang, T. A. Valiante, In vitro recordings of human neocortical oscillations, *Cerebral Cortex* **25**, 578–597 (2015).

38. N. W. Johnson, M. Özkan, A. P. Burgess, E. J. Prokic, K. A. Wafford, M. J. O'Neill, S. D. Greenhill, I. M. Stanford, G. L. Woodhall, Phase-amplitude coupled persistent theta and gamma oscillations in rat primary motor cortex in vitro, *Neuropharmacology* **119**, 141–156 (2017).

39. N. Rustamov, J. Humphries, A. Carter, E. C. Leuthardt, Theta-gamma coupling as a cortical biomarker of brain-computer interface-mediated motor recovery in chronic stroke, *Brain Commun* **4**, 1–18 (2022).

40. R. K. Spooner, T. W. Wilson, Cortical theta–gamma coupling governs the adaptive control of motor commands, *Brain Commun* **4**, 1–12 (2022).

41. A. B. L. Tort, R. Komorowski, H. Eichenbaum, N. Kopell, Measuring Phase-Amplitude Coupling Between Neuronal Oscillations of Different Frequencies, *Journal of Neurophysiology* **104**, 1195–1210 (2010).

42. A. B. L. Tort, M. A. Kramer, C. Thorn, D. J. Gibson, Y. Kubota, A. M. Graybiel, N. J. Kopell, Dynamic cross-frequency couplings of local field potential oscillations in rat striatum and hippocampus during performance of a T-maze task, *Proceedings of the National Academy of Sciences* **105**, 20517–20522 (2008).

43. C. Scheffzük, V. I. Kukushka, A. L. Vyssotski, A. Draguhn, A. B. L. Tort, J. Brankačk, Selective coupling between theta phase and neocortical fast gamma oscillations during REM-sleep in mice, *PLoS ONE* **6**, e28489 (2011).

44. J. A. Hoskins, L. J. Davis, The acute effect on levels of catecholamines and metabolites in brain, of a single dose of MPTP in 8 strains of mice, *Neuropharmacology* **28**, 1389–1397 (1989).

45. P.-O. Polack, J. Friedman, P. Golshani, Cellular mechanisms of brain state-dependent gain modulation in visual cortex, *Nature Neuroscience* **16**, 1331–1339 (2013).

46. J. Reimer, M. J. McGinley, Y. Liu, C. Rodenkirch, Q. Wang, D. A. McCormick, A. S. Tolias, Pupil fluctuations track rapid changes in adrenergic and cholinergic activity in cortex, *Nature Communications* **7**, 1–7 (1AD).

47. J. M. Fritschy, R. Grzanna, Selective effects of DSP-4 on locus coeruleus axons: are there pharmacologically different types of noradrenergic axons in the central nervous system? *Prog Brain Res* **88**, 257–268 (1991).

48. S. A. Thomas, B. T. Marck, R. D. Palmiter, A. M. Matsumoto, Restoration of Norepinephrine and Reversal of Phenotypes in Mice Lacking Dopamine fi-Hydroxylase, *J Neurochem* **70**, 20468–20476 (1998).

49. N. R. Jabir, C. K. Firoz, T. A. Zughaibi, M. A. Alsaadi, A. M. Abuzenadah, A. I. Al-Asmari, A. Alsaieedi, B. A. Ahmed, A. K. Ramu, S. Tabrez, A literature perspective on the pharmacological applications of yohimbine, *Annals of Medicine* **54**, 2849–2863 (2023).

50. D. Zhang, S. Chen, S. Xu, J. Wu, Y. Zhuang, W. Cao, X. Chen, X. Li, The clinical correlation between Alzheimer's disease and epilepsy, *Front. Neurol.* **13**, 922535 (2022).

51. D. Schijven, R. Stevelink, M. McCormack, W. van Rheenen, J. J. Luykx, Bobby P.C. Koeleman, J. H. Veldink, P. M. A. G. Consortium, I. L. A. E. C. O. C. Epilepsies, Analysis of shared common genetic risk between amyotrophic lateral sclerosis and epilepsy, *Neurobiology of Aging* **92**, 153.e1–153.e5 (2020).

52. A. M. García-Cabrero, R. Guerrero-López, B. G. Giráldez, M. Llorens-Martín, J. Ávila, J. M. Serratosa, M. P. Sánchez, Hyperexcitability and epileptic seizures in a model of frontotemporal dementia, *Neurobiology of Disease* **58**, 200–208 (2013).

53. V. Gomez-Murcia, U. Sandau, B. Ferry, S. Parrot, C. Laurent, M. Basquin, L. Buée, D. Boison, D. Blum, Hyperexcitability and seizures in the THY-Tau22 mouse model of tauopathy, *Neurobiology of Aging* **94**, 265–270 (2020).

54. Y. Salimpour, Cross-Frequency Coupling Based Neuromodulation for Treating Neurological Disorders, *Frontiers in Neuroscience* **13**, 125 (2019).

55. A. Malekshahi, U. Chaudhary, A. Jaramillo-Gonzalez, A. Lucas Luna, A. Rana, A. Tonin, N. Birbaumer, S. Gais, Sleep in the completely locked-in state (CLIS) in amyotrophic lateral sclerosis, *Sleep* **42** (2019).

56. A. Secco, A. Tonin, A. Rana, A. Jaramillo-Gonzalez, M. Khalili-Ardali, N. Birbaumer, U. Chaudhary, EEG power spectral density in locked-in and completely locked-in state patients: a longitudinal study, *Cognitive Neurodynamics* **15**, 473–480 (2020).

57. Q. Gu, Neuromodulatory transmitter systems in the cortex and their role in cortical plasticity, *Neuroscience* **111**, 815–835 (2002).

58. E. Sofic, P. Riederer, W. Gsell, M. Gavranovic, A. Schmidtke, K. Jellinger, Biogenic amines and metabolites in spinal cord of patients with Parkinson's disease and amyotrophic lateral sclerosis, *J Neural Transm* **3**, 133–142 (1991).

59. O. Bertel, S. Malessa, E. Sluga, O. Hornykiewicz, Amyotrophic lateral sclerosis: changes of noradrenergic and serotonergic transmitter systems in the spinal cord, *Brain Research* **566**, 54–60 (1991).

60. B. R. Brooks, M. G. Ziegler, C. R. Lake, J. H. Wood, S. J. Enna, W. K. Engel, Cerebrospinal Fluid Norepinephrine and Free Gamma-Aminobutyric Acid in Amyotrophic Lateral Sclerosis, *Brain Research Bulletin* **5**, 765–768 (1980).

61. M. G. Ziegler, B. R. Brooks, C. R. Lake, J. H. Wood, S. J. Enna, Norepinephrine and gamma-aminobutyric acid in amyotrophic lateral sclerosis, *Neurology* **30** (1980).

62. V. P. Barkhatova, I. A. Zavalishin, A. V. Kostiuk, E. G. Demina, T. A. Moskvitina, Neurotransmitter changes in amyotrophic lateral sclerosis, *Zh Nevrol Psikhiatr Im S S Korsakova* **96**, 78–85 (1996).

752 63. W. Hoogendijk, C. W. Pool, D. Troost, E. van Zwieten, undefined author, D. F. Swaab, Image
753 analyser-assisted morphometry of the locus coeruleus in Alzheimer“s disease, Parkinson”s disease and
754 amyotrophic lateral sclerosis, *Brain : a journal of neurology* **118**, 131–143 (1995).

755 64. R. W. Orrell, A. W. King, D. A. Hilton, M. J. Campbell, R. J. Lane, J. S. de Belleroche, Familial
756 amyotrophic lateral sclerosis with a point mutation of SOD-1: intrafamilial heterogeneity of disease
757 duration associated with neurofibrillary tangles, *Journal of Neurology, Neurosurgery & Psychiatry* **59**,
758 266–270 (1995).

759 65. J. Brettschneider, K. Del Tredici, J. B. Toledo, J. L. Robinson, D. J. Irwin, M. Grossman, E. Suh, V.
760 M. Van Deerlin, E. M. Wood, Y. Baek, L. Kwong, E. B. Lee, L. Elman, L. McCluskey, L. Fang, S.
761 Feldengut, A. C. Ludolph, V. M. Y. Lee, H. Braak, J. Q. Trojanowski, Stages of pTDP-43 pathology
762 in amyotrophic lateral sclerosis, *Ann Neurol.* **74**, 20–38 (2013).

763 66. M. Van Egroo, E. Koshmanova, G. Vandewalle, H. I. L. Jacobs, Importance of the locus coeruleus-
764 norepinephrine system in sleep- wake regulation: Implications for aging and Alzheimer's disease,
765 *Sleep Medicine Reviews* **62**, 101592 (2022).

766 67. H. Salgado, M. Treviño, M. Atzori, Layer- and area-specific actions of norepinephrine on cortical
767 synaptic transmission, *Brain Research* **1641**, 163–176 (2016).

768 68. B. Feinstein, C. A. Gleason, B. Libet, Stimulation of locus coeruleus in man. Preliminary trials for
769 spasticity and epilepsy, *Stereotact Funct Neurosurg* **52**, 26–41 (1989).

770 69. G. K. Weiss, J. Lewis, C. Jimenez-Rivera, A. Vigil, M. E. Corcoran, Antikindling effects of locus
771 coeruleus stimulation: mediation by ascending noradrenergic projections, *Experimental Neurology*
772 **108**, 136–140 (1990).

773 70. G. Ferraro, P. Sardo, M. Sabatino, G. Caravaglios, V. La Grutta, Anticonvulsant activity of the
774 noradrenergic locus coeruleus system: role of beta mediation, *Neuroscience Letters* **169**, 93–96 (1994).

775 71. P. K. Mishra, R. L. Burger, A. F. Bettendorf, R. A. Browning, P. C. Jobe, Role of norepinephrine in
776 forebrain and brainstem seizures: chemical lesioning of locus ceruleus with DSP4, *Experimental*
777 *Neurology* **125**, 58–64 (1994).

778 72. P. Szot, D. Weinshenker, S. S. White, C. A. Robbins, N. C. Rust, P. A. Schwartzkroin, R. D. Palmiter,
779 Norepinephrine-deficient mice have increased susceptibility to seizure-inducing stimuli, *Journal of*
780 *Neuroscience* **19**, 10985–10992 (1999).

781 73. V. A. Nazarova, A. V. Sokolov, V. N. Chubarev, V. V. Tarasov, H. B. Schiöth, Treatment of ADHD:
782 Drugs, psychological therapies, devices, complementary and alternative methods as well as the trends
783 in clinical trials, *Front Pharmacol* **13**, 1066988 (2022).

784 74. A. Montoya, R. Bruins, M. A. Katzman, P. Blier, The noradrenergic paradox: implications in the
785 management of depression and anxiety, *Neuropsychiatr Dis Treat* **12**, 541–557 (2016).

786 75. M. E. Heidari, J. Nadali, A. Parouhan, M. Azarafraz, S. M. tabatabai, S. S. N. Irvani, F. eskandari, A.
787 Gharebaghi, Prevalence of depression among amyotrophic lateral sclerosis (ALS) patients: A
788 systematic review and meta-analysis , *Journal of Affective Disorders* **287**, 182–190 (2021).

76. J. M. Statland, D. Moore, Y. Wang, M. Walsh, T. Mozaffar, L. Elman, S. P. Nations, H. Mitsumoto, J. A. Fernandes, D. Saperstein, G. Hayat, L. Herbelin, C. Karam, J. Katz, H. M. Wilkins, A. Agbas, R. H. Swerdlow, R. M. Santella, M. M. Dimachkie, R. J. Barohn, Rasagiline Investigators of the Muscle Study Group and Western ALS Consortium, Rasagiline for amyotrophic lateral sclerosis: A randomized, controlled trial, *Muscle Nerve* **59**, 201–207 (2019).

77. E. Dalla Bella, E. Bersano, G. Antonini, G. Borghero, M. Capasso, C. Caponnetto, A. Chiò, M. Corbo, M. Filosto, F. Giannini, R. Spataro, C. Lunetta, J. Mandrioli, S. Messina, M. R. Monsurrò, G. Mora, N. Riva, R. Rizzi, G. Siciliano, V. Silani, I. Simone, G. Sorarù, V. Tugnoli, L. Verriello, P. Volanti, R. Furlan, J. M. Nolan, E. Abgueguen, I. Tramacere, G. Lauria, The unfolded protein response in amyotrophic later sclerosis: results of a phase 2 trial, *Brain : a journal of neurology* **144**, 2635–2647 (2021).

78. X. Li, D. D. Koeberl, M. W. Lutz, R. Bedlack, Clenbuterol Treatment Is Safe and Associated With Slowed Disease Progression in a Small Open-Label Trial in Patients With Amyotrophic Lateral Sclerosis, *J Clin Neuromuscul Dis* **24**, 214–221 (2023).

79. K. Kam, Á. M. Duffy, J. Moretto, J. J. LaFrancois, H. E. Scharfman, Interictal spikes during sleep are an early defect in the Tg2576 mouse model of, *Scientific Reports*, 1–16 (2016).

80. H. Bokil, P. Andrews, J. E. Kulkarni, S. Mehta, P. P. Mitra, Chronux: a platform for analyzing neural signals, *Journal of Neuroscience Methods* **192**, 146–151 (2010).

81. B. R. Brooks, R. G. Miller, M. Swash, T. L. Munsat, World Federation of Neurology Research Group on Motor Neuron Diseases, in (2000), vol. 1, pp. 293–299.

82. S. Sangari, I. Peyre, A. Lackmy-Vallée, E. Bayen, P.-F. Pradat, V. Marchand-Pauvert, Transient increase in recurrent inhibition in amyotrophic lateral sclerosis as a putative protection from neurodegeneration, *Acta Physiol* **234**, e13758 (2022).

83. A. Delorme, S. Makeig, EEGLAB: an open source toolbox for analysis of single-trial EEG dynamics including independent component analysis, *Journal of Neuroscience Methods* **134**, 9–21 (2004).

84. O. Bertrand, F. Perrin, J. Pernier, A theoretical justification of the average reference in topographic evoked potential studies, *Electroencephalography and Clinical Neurophysiology* **62**, 462–464 (1985).

85. A. Delorme, T. Sejnowski, S. Makeig, Enhanced detection of artifacts in EEG data using higher-order statistics and independent component analysis, *NeuroImage* **34**, 1443–1449 (2007).

86. S. Makeig, A. J. Bell, T.-P. Jung, T. J. Sejnowski, Complex independent component analysis of frequency-domain electroencephalographic data, *NIPS* **16**, 1311–1323 (1995).

87. R. Martínez-Cancino, J. Heng, A. Delorme, K. Kreutz-Delgado, R. C. Sotero, S. Makeig, Measuring transient phase-amplitude coupling using local mutual information, *NeuroImage* **185**, 361–378 (2019).

88. M. Kremer, I. Yalcin, Y. Goumon, X. Wurtz, L. Nexon, D. Daniel, S. Megat, R. A. Ceredig, C. Ernst, G. Turecki, V. Chavant, J.-F. Théroux, A. Lacaud, L.-E. Joganah, V. Lelievre, D. Massotte, P.-E. Lutz, R. Gilsbach, E. Salvat, M. Barrot, A Dual Noradrenergic Mechanism for the Relief of

Neuropathic Allodynia by the Antidepressant Drugs Duloxetine and Amitriptyline, *Journal of Neuroscience* **38**, 9934–9954 (2018).

89. D. L. Lin, W. T. Chang, T. L. Kuo, R. H. Liu, Chemical derivatization and the selection of deuterated internal standard for quantitative determination--methamphetamine example, *J Anal Toxicol* **24**, 275–280 (2000).

90. S. Liebscher, G. B. Keller, P. M. Goltstein, T. Bonhoeffer, M. Hübener, Selective Persistence of Sensorimotor Mismatch Signals in Visual Cortex of Behaving Alzheimer's Disease Mice, *Current Biology* **26**, 956–964 (2016).

91. A. Dobin, C. A. Davis, F. Schlesinger, J. Drenkow, C. Zaleski, S. Jha, P. Batut, M. Chaisson, T. R. Gingeras, STAR: ultrafast universal RNA-seq aligner, *Bioinformatics* **29**, 15–21 (2013).

92. S. Orjuela, R. Huang, K. M. Hembach, M. D. Robinson, C. Soneson, ARMOR: An Automated Reproducible MOdular Workflow for Preprocessing and Differential Analysis of RNA-seq Data, *G3 (Bethesda)* **9**, 2089–2096 (2019).

93. C. Rouaux, I. Panteleeva, F. Rene, J.-L. Gonzalez de Aguilar, A. Echaniz-Laguna, L. Dupuis, Y. Menger, A.-L. Boutillier, J.-P. Loeffler, Sodium valproate exerts neuroprotective effects in vivo through CREB-binding protein-dependent mechanisms but does not improve survival in an amyotrophic lateral sclerosis mouse model, *Journal of Neuroscience* **27**, 5535–5545 (2007).

Figures legends

Figure 1: *Sod1*^{G86R} and *Fus*$^{\Delta NLS/+}$ mice exhibit cortical hyperexcitability. (**A, B**) Genetic background and time course of disease onset and progression in the *Sod1*^{G86R} and *Fus*$^{\Delta NLS/+}$ mouse models of ALS. (**C**) Schematic representation of the positioning of subdural electrodes used for ECoG. (**D, E**) Representative ECoG traces prior to (10 min in total, only 2min are represented) and following (20min) a single injection of 30mg/kg of PTZ of *Sod1*^{G86R} (**D**) and *Fus*$^{\Delta NLS/+}$ (**E**) mice and control littermates. (**F**) Quantification of the number of epileptiform-like events displayed by *Sod1*^{G86R} and controls upon PTZ administration. (**G**) Latency to first epileptiform-like event upon PTZ injection of *Sod1*^{G86R} mice and their WT littermates. (**H**) Quantification of the number of epileptiform-like events displayed by *Fus*$^{\Delta NLS/+}$ mice and controls during the first 10 min that immediately followed PTZ administration. (**I**) Latency to first epileptiform-like event upon PTZ injection of *Fus*$^{\Delta NLS/+}$ mice and their WT littermates. n=5 WT and 5 *Sod1*^{G86R} female mice; n=4 WT females and 4 *Fus*$^{\Delta NLS/+}$ female mice. Two-sided unpaired Student's t-test; *p<0.05; ** p<0.01; **** p<0.0001.

Figure 2: *Sod1*^{G86R} and *Fus*$^{\Delta NLS/+}$ mice display presymptomatic and sustained decreased T-HG PAC during REM sleep. (**A**) Schematic representation of theta (red) and gamma (bue) waves and theta-gamma

PAC (right). (**B, C**) Averaged co-modulation phase-amplitude maps from 45-day-old WT and *Sod1*^{G86R} mice (**B**) and 3 month-old WT and *Fus*$^{\Delta NLS/+}$ mice (**C**) during REM sleep. Colour gradients represent the modulation index (MI); HG: high gamma; LG: low gamma. (**D, E**) Graphs representing the MI across frequencies in 45 day-old WT and *Sod1*^{G86R} mice (**D**) and 3 month-old WT and *Fus*$^{\Delta NLS/+}$ mice (**E**) during REM sleep. (**F, G**) Graphs representing the longitudinal T-LG PAC of WT and *Sod1*^{G86R} mice (**F**) and WT and *Fus*$^{\Delta NLS/+}$ mice (**G**) during REM sleep. (**H, I**) Graphs representing the longitudinal T-HG PAC of WT and *Sod1*^{G86R} mice (**H**) and WT and *Fus*$^{\Delta NLS/+}$ mice (**I**) during REM sleep. n=13 WT and 10 *Sod1*^{G86R} male mice; n=6 WT and 5 *Fus*$^{\Delta NLS/+}$ male mice. Two-way ANOVA (**D, E**) or mixed-effect analysis (**F, G, H, I**) followed by multiple comparisons test. #p<0.05; ## p<0.01; #### p<0.0001 for genotype effect in two-way ANOVA or mixed-effect analysis and *p<0.05; **p<0.01; ***p<0.001 in pairwise comparisons with age-matched WT controls.

Figure 3: *Sod1*^{G86R} mice display presymptomatic and sustained alteration of T-LG PAC during active wake. (**A, B**) Averaged co-modulation phase-amplitude maps from 45 day-old WT and *Sod1*^{G86R} mice (**A**) and 3 month-old WT and *Fus*$^{\Delta NLS/+}$ mice (**B**) during active wake. Colour gradients represent the modulation index (MI), HG: high gamma, LG: low gamma. (**C, D**) Graphs representing the MI across frequencies in 45 day-old WT and *Sod1*^{G86R} mice (**C**) and 3 month-old WT and *Fus*$^{\Delta NLS/+}$ mice (**D**) during active wake. (**E, F**) Graphs representing the longitudinal T-LG PAC of WT and *Sod1*^{G86R} mice from presymptomatic ages (45 and 60 days) to disease end stage (105 days) (**E**) and WT and *Fus*$^{\Delta NLS/+}$ mice from the presymptomatic age of 3 months until the symptomatic age of 11 months (**F**) during active wake. n=13 WT and 10 *Sod1*^{G86R} male mice; n = 6 WT and 5 *Fus*$^{\Delta NLS/+}$ male mice. Two-way ANOVA (**C, D**) or mixed-effect analysis (**E, F**) followed by multiple comparisons test. ### p<0.001 for genotype effect in two-way ANOVA of mixed-effect analysis and *p<0.05; **p<0.01; ***p<0.001 in pairwise comparisons with age-matched WT controls.

Figure 4: Sporadic ALS patients display decreased theta-gamma PAC over the left sensory motor cortex during EC rsEEG. (**A**) Schematic representation of the positioning of the electrodes of interest, over the sensorimotor areas (C_3, C_4) and along the interhemispheric sulcus: (F_z, C_z, P_z) (left), and schematic representation of theta-gamma PAC (right). (**B**) Representative co-modulation phase-amplitude maps from one representative healthy participant (Control) and one representative patient (ALS). Colour gradients represent the modulation index (MI). (**C**) Graphs representing the mean MI of healthy individuals (grey) and sporadic ALS patients (coral) in rsEEG. (**D**) Correlation between C_3 mean MI of ALS patients and their disease progression rate. (**E**) Graph representing the C_3 mean MI of ALS patients subdivided between fast versus slow progressors. n=26 controls and 26 ALS patients. Repeated-measures linear mixed-effect model

(rmLMM) followed by multiple comparisons test with ££££ p<0.0001 comparing EO and EC conditions; #p<0.05 between patients and controls in either EO or EC condition, and **p<0.01 and ****p<0.001 in pairwise comparisons between healthy controls and ALS patients for a given condition (EO or closed) and electrode (**C**). Multiple regression analysis with *p<0.05 (**D**). Two-tailed unpaired t-test with *p<0.05 (**E**).

Figure 5: The motor cortex of *Sod1^{G86R}* and *Fus$^{\Delta NLS/+}$* mice exhibits altered noradrenaline (NA) homeostasis. (**A**) NA concentration measured by LC-MS in the motor cortex of 45, 60 and 90-day-old *Sod1^{G86R}* and 4-month-old *Fus$^{\Delta NLS/+}$* female mice and their respective controls (n=9 WT and 8 *Sod1^{G86R}* at 45 days, 10 WT and 10 *Sod1^{G86R}* at 60 days and 8 WT and 8 *Sod1^{G86R}* at 90 days; n=8 WT and 8 *Fus$^{\Delta NLS/+}$*). (**B**) Representative images of the cerebral cortex of 90-day-old WT and *Sod1^{G86R}* mice and 4-month-old WT and *Fus$^{\Delta NLS/+}$* mice following DBH immunolabelling. Scale bars: 500µm and 100µm in close-ups. (**C**) Quantifications of cortical DBH-positive noradrenergic fibre density in 45, 60 and 90-day-old *Sod1^{G86R}* female mice and controls, and 4-month-old *Fus$^{\Delta NLS/+}$* female mice and controls (n=6 WT and 5 *Sod1^{G86R}* at 45 days, 6 WT and 4 *Sod1^{G86R}* at 60 days, and 5 WT and 5 *Sod1^{G86R}* at 90 days; n=5 WT and 5 *Fus$^{\Delta NLS/+}$*). (**D, E, F**) Relative mRNA expression levels of *Adra2a, Adra2b, Adrb2* in the motor cortex of 45, 60 and 90-day-old *Sod1^{G86R}* and 4 month-old *Fus$^{\Delta NLS/+}$* female mice and their respective controls (n=9 WT and 8 *Sod1^{G86R}* at 45 days, 8 WT and 8 *Sod1^{G86R}* at 60 days, and 8 WT and 8 *Sod1^{G86R}* at 90 days; n=8 WT and 8 *Fus$^{\Delta NLS/+}$*). (**G, H, I**) Quantification of adrenergic receptors 2A, 2B and B2 revealed by western blot in motor cortex extracts from 90-day-old *Sod1^{G86R}* and 6 month-old *Fus$^{\Delta NLS/+}$* mice and their respective controls (n=4 female mice per group). (**J, K, L**) Representative images of the cerebral cortex (left) of 60-day-old WT and *Sod1^{G86R}* mice immunolabelling to reveal adrenergic receptors 2A (**J**), 2B (**K**) and B2 (**L**) (white) along with CTIP2-, PV- and SST-positive neurons (red), scale bars: 10µm, and quantification of the receptor expression (right) based on fluorescence in the corresponding graphs to the left. ((n=3 female mice per group). *Sod1^{G86R}* mRNA samples were analysed by two-way ANOVA followed by multiple comparisons test, *Fus$^{\Delta NLS/+}$* mRNA samples & protein expression for *Sod1^{G86R}* and *Fus$^{\Delta NLS/+}$* were analysed by two-sided unpaired Student's t-test. #p<0.05; ##p<0.01; ####p<0.0001 for genotype effect in two-way ANOVA and *p<0.05; **p<0.01; ***p<0.001; ****p<0.0001 in pairwise comparisons with age-matched WT controls.

Figure 6. Release of NA in behaving mice is strongly diminished in *SOD1^{G93A}* mice. (**A**) NA release associated with locomotion was assessed by in vivo two-photon imaging of the AAV mediated expression of the noradrenaline indicator GRABNE1m in headfixed mice running on spherical treadmill. Mean projection of an example field of view (FOV) from a WT mouse. Superimposed grid demonstrates location and size of regions of interest (ROIs). Representative ROI referenced by time with respect to locomotion

onset shown on the right. (**B**) Heat map of fluorescent traces of all ROIs in an example FOV of a TW mouse shown in (A) across the entire recording session referenced by running speed (blue trace on top) and binary running epochs (blue area). (**C**) Averaged running-associated response of each ROI for the same FOV shown in (b). (**D**) Average population response to locomotion onset of all FOVs in WT (black) and *SOD1*^{G93A} mice (red) (p=0.0023, two-sided Student's t-test for the area under the curve [grey area], WT: 20 FOV, 2 male and 2 female mice; *SOD1*^{G93A}: 20 FOV, 2 male and 3 female mice). (**e**) Speed-dependent tuning curve of the locomotion-associated NA release (maximum value within -0.5 to 1.5s of running onset, grey area) in WT (y=0.48x+0.01, R^2=0.91, slope p=0.012, two-sided Student's t-test) and *SOD1*^{G93A} mice (y=0.13x+0.003, R^2=0.482, slope p=0.19, slope difference between WT and *SOD1*^{G93A} p=0.0148, two-sided unpaired Student's t-test). (**F**) Correlogram depicting pairwise correlations (Pearson's correlation coefficient) of individual ROIs in the same FOV shown in b, c. (**G**) Pairwise ROI correlations do not differ between WT and *SOD1*^{G93A} mice. *p<0.05, **p<0.01.

Figure 7: **Post-mortem motor cortex and LC from ALS patients display decreased NA concentration, along with altered expression of genes involved in noradrenegeric signalling.** (**A**) LC-MS quantification of NA in the post-mortem motor cortex, LC and spinal cord of ALS patients (coral) and age-matched healthy controls (grey). Motor cortex: n=7 healthy controls, 9 ALS patients; LC: n=3 healthy controls, 3 ALS patients; spinal cord: n=3 healthy controls, 6 ALS patients. One-sided unpaired Student's t-test. *p<0.05; **p<0.01; ns: non-significant. (**B**) Correlation between NA in post-mortem motor cortices from healthy controls (left, grey) or ALS patients (right, coral) and their age at death. (**C**) Relative mRNA expression of genes involved in noradrenergic signalling in the post-mortem motor and frontal cortices of ALS patients (coral) and age-matched healthy controls (grey). n=29 healthy controls and 27 ALS patients. Differential gene expression analysis; **FDR<0.01; ***FDR<0.001.

Figure 8: NA critically regulates cortical hyperexcitability and theta-gamma PAC. (**A**) Schematic representation of the experimental paradigm: PTZ was administered in WT mice prior to each ECoG recording, and two EcoG recordings were performed 38 days apart from each other, before, and 8 days after DSP-4 administration to induce noradrenergic fibre degeneration and cortical NA depletion. (**B**) Representative ECoG traces following a single injection of PTZ of WT animals prior to or after DSP-4 administration. (**C**) Before-after graph representing the number of epileptiform-like events triggered by PTZ before and after DSP-4 administration (n=4 WT female mice); two-sided paired Student's t-test; *p<0.05. (**D**) Schematic representation of the experimental paradigm: two EcoG recordings were performed

48h apart from each other, before and after DSP-4 administration. (**E**) Before-after graph representing the MI of T-HG PAC during REM sleep before and after DSP-4 administration (n=5 WT animals); two-sided paired Student's t-test; **p<0.01. (**F**) Schematic representation of the experimental paradigm: two EcoG recordings were performed 12 h apart from each other, before and after L-DOPS and Benserazide administration. (**G**) Before-after graph representing the MI of T-HG PAC during REM sleep before and after L-DOPS and Benserazide administration in *Sod1*^{G86R} mice and their WT littermates (n=4 WT and 5 *Sod1*^{G86R} female mice); two-sided paired Student's t-test; *p<0.05; ns: non-significant. (**H**) Schematic representation of the experimental paradigm: five EcoG recordings were performed 10 days apart from each other, before, and during daily yohimbine administration. (**I**) Graph representing the MI of T-HG PAC during REM sleep before and after yohimbine administration in *Sod1*^{G86R} mice and their WT littermates (n=7 WT and 6 *Sod1*^{G86R} female mice); two-way ANOVA followed by multiple comparisons test; *p<0.05; **p<0.01; in pairwise comparisons between untreated and treated *Sod1*^{G86R} mice.

Table 1: Clinical characteristics of the sporadic ALS patients included in the rsEEG study.

List of the patients included in the resting state EEG study and their age at recording, handedness, and main clinical features. LL: lower limb onset; B: bulbar onset; UL: upper limb onset; ALSFRS-r: mean score rectified ALS functional rating; UMN: upper motoneuron score. ALSFRS-r and UMN have arbitrary units. Disease duration is expressed in months. Progression rate represent the amount of lost points on the ALSFRS-r scale divided by the disease duration, and is expressed in month^{-1}. Calculation of the mean progression rate of the group of ALS patients allowed their segregation between fast (individual progression rate>mean progression rate) and slow progressors (individual progression rate<mean progression rate).

983

Patients	Age	Handedness	Site of Onset	Disease duration	ALS-FRSR	Progression rate	Defined Progression rate	UMN score
ALS 1	73	R	LL	60	37	0,183	Slow	0
ALS 2	62	L	B	36	34	0,389	Slow	3
ALS 3	63	R	LL	18	41	0,389	Slow	2
ALS 4	52	R	LL	45	36	0,267	Slow	3
ALS 5	45	R	UL	10	44	0,400	Slow	2
ALS 6	63	L	LL	15	44	0,267	Slow	3
ALS 7	41	R	UL	14	43	0,357	Slow	2
ALS 8	70	L	UL	36	40	0,222	Slow	0
ALS 9	80	R	LL	15	42	0,400	Slow	0
ALS 10	66	R	UL	8	36	1,500	Fast	2
ALS 11	74	R	B	8	34	1,750	Fast	3
ALS 12	77	R	LL	8	43	0,625	Fast	0
ALS 13	61	R	LL	76	41	0,092	Slow	4
ALS 14	72	R	LL	37	34	0,378	Slow	2
ALS 15	29	R	UL	22	38	0,455	Fast	3
ALS 16	73	R	B	11	43	0,455	Fast	3
ALS 17	67	R	B	6	47	0,167	Slow	3
ALS 18	59	R	LL	3	40	2,667	Fast	0
ALS 19	52	R	B	43	39	0,209	Slow	3
ALS 20	46	R	UL	31	35	0,419	Fast	3
ALS 21	68	R	UL	20	47	0,050	Slow	1
ALS 22	68	R	LL	9	40	0,889	Fast	0
ALS 23	42	R	UP	7	43	0,714	Fast	2
ALS 24	57	R	UP	9	35	1,444	Fast	3
ALS 25	61	R	LL	8	40	1,000	Fast	4
ALS 26	52	R	LL	7	38	1,429	Fast	4

984

985

Acknowledgments

We are extremely grateful to all ALS patients and healthy volunteers who participated in the study. The authors are thankful to Annie Picchinenna, and Claudia de Tapia for technical assistance (Inserm U1329, Université de Strasbourg), Dr. Alexandra Lackmy-Vallée (LIB, Sorbonne Université) and Christophe Gitton (CENIR-EEG/MEG platform, Brain Institute ICM, Paris) for their technical assistance to collect rsEEG, Maximilien Chaumon (CENIR-EEG/MEG platform, Brain Institute ICM, Paris) for his valuable help for EEG preprocessing and Dr A. Giron (LIB, Sorbonne Université) for his valuable advices for rsEEG statistical analysis. The authors thank the Hôpital de la Pitié-Salpêtrière and Brainbank Neuro-CEB Neuropathology Network [Dr Franck Letournel (CHU Angers), Dr Marie-Laure Martin-Négrier (CHU Bordeaux), Pr Françoise Chapon (CHU Caen), Pr Catherine Godfraind (CHU Clermont-Ferrand), Pr Claude-Alain Maurage (CHU Lille), Dr Vincent Deramecourt (CHU Lille), Dr David Meyronnet (CHU Lyon), Dr Nathalie Streichenberger (CHU Lyon), Dr André Maues de Paula (CHU Marseille), Pr Valérie Rigau (CHU Montpellier), Dr Fanny Vandenbos-Burel (Nice), Pr Charles Duyckaerts (CHU PS Paris), Pr Danielle Seilhean (CHU PS, Paris), Dr Susana Boluda (CHU PS, Paris), Dr Isabelle Plu (CHU PS, Paris), Dr Serge Milin (CHU Poitiers), Dr Dan Christian Chiforeanu (CHU Rennes), Pr Annie Laquerrière (CHU Rouen), Dr Béatrice Lannes (CHU Strasbourg)] for providing human tissues.

Funding

The work has been supported by:

European Research Council starting grant #639737 (CR), Association pour la Recherche sur la Sclérose Latérale Amyotrophique (CR, RG), Agence Nationale de la Recherche- Deutsche Forschungsgemeinschaft ANR-21-CE37-0033-01 (CR, SL, VMP, RG), Post-doctoral fellowship from the Association Française contre les Myopathies-Téléthon #21993 (JSZ), PhD fellowships from the French Ministry of Scientific Research and Innovation (CB, AB), 4rth year PhD fellowship from the Association pour la Recherche sur la Sclérose Latérale Amyotrophique (ARSLA) (CB), Cluster for Systems Neurology -EXC 2145 SyNergy- ID 390857198 (SL), The Emmy Noether Program of the German Research Foundation (SL), Deutsche Gesellschaft für Muskelkranke e.V. (SL), The Brainbank Neuro-CEB Neuropathology Network is supported by the following associations: ARSLA, CSC, France DFT, Fondation ARSEP, Fondation Vaincre Alzheimer, France Parkinson, German Research Foundation under Germany's Excellence Strategy within the framework of the Munich

Author contributions

CR, SL and VMP conceptualized the study, with intellectual contributions from LD and FR. JSZ and GSL performed ECoG recordings and analyzed the data together with VD, JG, SJG, JS, and MF and the expertise of RG. PFP enrolled ALS patients and controls, VMP performed EEG recordings. AB and VA performed LC-MS measurements with the expertise of YG. AB, SDG, CG, MT and SD performed qPCR, western blot and immunofluorescence experiments and AB, SDG, SD, analyzed the data with image analyses tools designed by PK. GSL and CG treated the animals and performed the survival analyses. ZG processed human tissue samples. SM performed transcriptomic analysis on human data. EL, WK, XY performed in vivo two-photon imaging; XY, SL analyzed and visualized in vivo 2p imaging data. CR, SL and VMP supervised the study and secured funding. CR and SL prepared the figures. The manuscript was drafted by CR, SL and VMP and reviewed and accepted by all authors.

Competing interests

Authors declare that they have no competing interests.

Data and materials availability

All data associated with this study are present in the paper or the Supplementary Materials. The patient raw datasets cannot be made publicly available due to the data protection concerns regarding potentially identifying and sensitive patient information. EEG raw data from the clinical study can be made available to qualified researchers from V. Marchand-Pauvert and PF. Pradat, in agreement with the INSERM and the French National Committee for the Protection of Individuals.

Noradrenaline deficiency as a driver of cortical hyperexcitability in amyotrophic lateral sclerosis

Scekic-Zahirovic‡, Benetton‡, Aurore Brunet‡, et al.,

SUPPLEMENTARY MATERIALS AND METHODS

Animals

Animals were housed with up to four littermates of the same sex with a regular 12-hour light and dark cycle, and were given access to water and standard laboratory rodent food ad libitum. Male and female *Sod1*^{G86R} and *Fus*$^{\Delta NLS/+}$ along with their control littermates were used in this study *(29, 30)*. Male and female *SOD1*^{G93A} transgenic mice (B6.Cg-Tg(SOD1*G93A)1Gur/J; Strain #:004435, Jackson Laboratory, maintained on a C57Bl/6J background) and WT littermates were used for monitoring NA release during locomotion by 2-photon microscopy.

Drugs

PTZ (P6500), DSP-4 (C8417), Benserazide (B7283) and yohimbine (Y3125) were purchased from Merck, and L-DOPS (S3041) from Selleck Chemicals.

Electrocorticography, and PAC analyses in mice

Surgery. Electrode implantation was performed as previously described *(79)* with modifications. 40-day-old mice were deeply anesthetized with 4% isoflurane (Piramal Critical Care) and placed on a stereotaxic frame (World Precision Instruments). Lidocaine (CEVA) was injected subcutaneously to provide local anaesthesia. The skull was exposed and four epidural screw electrodes (Bilaney) were positioned through the skull: one reference electrode 0.5 mm anterior to Bregma, close to the midline; two recording electrodes 2.5mm posterior to Bregma, 2mm lateral to the midline; one ground electrode 6.5mm posterior to Bregma, close to the midline. Two home-made electromyography (EMG) electrodes were placed within the deep muscles of the neck. All electrodes were secured using superbond (Sun Medical) and connected to a 6-pin connector (Bilaney) centred over the skull and secured with dental cement (Paladur). Animals were returned to their home cage and monitored daily until the first recording, at least 5 days after surgery.

Recordings. ECoG and EMG signals were recorded on LabChart 5 (ADInstruments). ECoG signals were acquired at a sampling rate of 2,000 Hz and bandpass filtered at 500 Hz (ADInstruments). Videos were simultaneously recorded at around 25 frames/s, using an infrared LED camera (Sony). For longitudinal recordings, mice were recorded for 24h every other week (*Sod1*^{G86R}) or every other month (*Fus*$^{\Delta NLS/+}$). DSP-4 (50mg/kg i.p.) injected WT mice were recorded during 24h before DSP-4 injection, and either 2 or 8 days after DSP-4 injection. *Sod1*^{G86R} mice and WT injected with L-DOPS (0.5 mg/g i.p.) and benserazide (0.125 mg/g i.p.) were recorded for 24h before injection and 12h after injection. Only the first 12h of these recordings were analysed. Additional *Sod1*^{G86R} mice and WT littermates were recorded for 24h prior to (45 days), and upon (55, 65, 75 and 85 days) yohimbine injections (6 mg/kg/d s.c.).

ECoG recording analyses. ECoG recordings were analysed using custom-written scripts in Matlab R2018a (MathWorks). Basic pre-processing of ECoG included denoising of slow variations and 50Hz (and harmonics up to 200Hz) electrical noise due to the single-phase power supply (Chronux Matlab toolbox) *(80)* and down sampling to 1kHz. Epochs of active wakefulness (aW), slow wave sleep (SWS) and rapid eye movement (REM) sleep, were identified based on ECoG characteristics (delta power, theta-delta ratio, sigma power) together with EMG and video recordings. Power spectra were calculated using the multitaper method (Chronux toolbox) as previously described *(17)* and the modulation index (MI) was calculated during wakefulness and REM sleep using Tort's method *(41)* as previously described *(17)*. The mean MI per gamma bin was calculated by fixing the phase frequency within the theta range. Single filtered theta traces were extracted with bandpass filters set 1 to +1Hz around the dominant theta frequency and calculated theta phase using the Hilbert transform. Gamma amplitude was calculated by taking the filtered

rectified gamma trace using the absolute value of the Hilbert-transformed gamma signal. MI was calculated between theta phase and each 10Hz frequency band spanning 10–200Hz.
For the PTZ susceptibility test, ECoG and video recordings were conducted on 85-day-old *Sod1*^{G86R} mice and 4-month-old *Fus*$^{\Delta NLS/+}$ mice and their respective WT littermates, over 20min:10min prior to and 20 min upon i.p. injection of 30 mg/kg of PTZ dissolved in NaCl 0.9%. Injection time was assessed on video recordings. ECoGs were analysed using a custom-written Python pipeline (Python Software Foundation; Python Language Reference, version 3.11. Available at http://www.python.org). ECoGs were notch-filtered to remove the powerline (50Hz) and its harmonics up to 200Hz. Each ECoG recording was normalized using a Z-score. Baseline Z-score were compared to the Z-score window after PTZ injection for each recording. Events in the PTZ window that were strictly greater than the baseline Z-score were counted, using a window discriminator of 4 times the baseline SD. Latency of the first event was also assessed. The pipeline is available on Zenodo (Guillot, S. J. (2023). EEG_events (2023.04.03-rc1). GitHub, Zenodo. https://doi.org/10.5281/zenodo.10656937).

Mouse tissue preparation
For liquid chromatography-mass spectrometry (LC-MS), qPCR and western blot analyses, mice were euthanized with a lethal i.p. dose of 120 mg/kg of pentobarbital sodium and phenytoin sodium and decapitated. The brains were dissected out and sliced in a cooled stainless-steel coronal brain matrix (Harvard Apparatus). 1 mm-thick sections were transferred under a stereomicroscope (Nikon) to micro-dissect the motor areas and hippocampus. Lumbar spinal cords (L1-L5) were dissected and split in two hemi-cords along the midline. Collected tissues were rapidly frozen in liquid nitrogen and stored at -80°C until used.

Patients
EEG procedures were performed on 26 patients with ALS (60.44±2.47 years old, range 28-79; 9 women/17 men, **Table 1**), all under riluzole, and an age- and sex-matched group of 26 healthy controls (63.42±2.08 years old, range 31-78; 8 women/18 men). The inclusion criteria for patients comprised *i)* probable or definite ALS diagnosis according to the revised El Escorial criteria *(81)*, confirmed by a senior neurologist of the ALS reference centre of the Pitié-Salpêtrière Hospital (P.-F.P, Paris, France) (mean score rectified ALS functional rating [ALSFRS-r]: 39.77±0.76, range 34-47, median 40), and *ii)* absence of medical conditions associated with peripheral neuropathy (such as diabetes, nerve entrapment, peripheral neuropathy). Progression rate was calculated by dividing the difference between the maximum (48) and the current ALSFRS-r score of the patient at visit divided by disease duration in months (mean disease duration 21.62±3.65 months, range 3-76; mean progression rate 0.66±0.12 point/month). Based on the mean progression rate, ALS patients were classified as slow fast progressors (progression rate ≤0.66 or >0.66 point/month). The UMN score was calculated as such: score to the modified Ashworth scale (0 if score<3 or 1 if score ≥ 3) + Babinski or Hoffmann sign (0= absent, 1=present) + evaluation of tendon reflex (0=normal or absent, 1=present in wasted muscle, 2=brisk) *(82)*. Patients with an incapacity to communicate due to anarthria were not included. Specific inclusion criteria for healthy controls were *i)* no history of neurological conditions and *ii)* no medication interfering with the normal functioning of the central nervous system, except riluzole.

EEG recordings and MI analyses in patients
EEG recordings (4-kHz sampling rate; bandpass 0.03-1330 Hz) were acquired on the Neuromag® TRIUX (Elekta) at the Centre of NeuroImaging Research (CENIR) of the Brain Institute (ICM, Pitié-Salpêtrière Hospital, Paris, France). An EEG cap with Ag/AgCl annular electrodes was placed according to the international 10-20 system (EasyCap GmbH) and positioned such that the C_z electrode was above the anatomical vertex. Water-soluble conducting-gel was injected in each electrode and impedance was checked individually (<10kΩ) before acquisition. Single-use pre-gelled Ag/AgCl electrodes (Ambu® Neuroline 720, Ballerup, Denmark) were placed over the right ear lobe to serve as reference electrode, and on the left scapula to serve as ground electrode. Non-neural signals comprising electrooculogram (EOG)

and electrocardiogram (ECG) were also recorded using single-use pre-gelled electrodes placed above and below the right eye to detect eye blinks, on the right and left temples for EOG to detect eye saccades, and on the right clavicle and the left part of lower abdomen (ECG). During the recordings, the participants were asked to stay relaxed and to limit movements as much as possible (such as eye movements, swallowing, jaw clenching). The protocol consisted of 2 runs of 5min of resting-state EEG (rs-EEG) spaced by 2min: a first run with the EO, fixing a cross, and a second run during with the EC. Analyses were performed using Matlab R2019b and EEGLAB 2021.1 *(83)* (MathWorks). EEG time series were resampled at 400 Hz, re-referenced (average reference) *(84)* and filtered (50-Hz notch filter and 2-60 Hz bandpass). Independent component analysis was performed to remove all non-neural signals from the EEG *(85, 86)*. The analysis was limited to the left and right sensorimotor cortex (C_3 and C_4, respectively) which are first affected in ALS, and nearby interhemispheric scissure (F_z, C_z, P_z). Power spectra density analysis (Fourier decomposition) of denoised EEG was undertaken to extract the mean maximum signal power in theta (4-8 Hz) and gamma (30-60 Hz) frequency bands. Higher frequencies within the gamma band (80-150Hz) were excluded due to noise and scalp muscle EMG contamination. The MI for theta-gamma PAC was calculated using Tort's method *(41)* as previously described *(87)*. The comodulograms between theta phase and gamma amplitude were constructed by subdividing each band into 100 (steps of 0.04Hz and 0.3-Hz for theta and gamma, respectively), and the mean MI was extracted.

Human samples

Autopsy samples from motor cortex, LC and spinal cord were obtained from the NeuroCEB biobank (https://www.neuroceb.org/fr/) for nine sporadic ALS patients and seven healthy controls. Patients or families had provided written informed consent. ALS diagnosis was based on the revised El Escorial criteria and confirmed after autopsy. During autopsy, tissue samples were frozen in liquid nitrogen. Use of the tissue for research was declared at the French ministry for research and higher education. LC samples were available for three sporadic ALS patients and three healthy controls. Spinal cords were available for six sporadic ALS patients and three healthy controls (**Supplementary Table 1**).

Liquid chromatography-mass spectrometry

Mass spectrometry analysis was performed as previously described *(88)*. Mouse tissues were homogenized with a Bio-Gen PRO200 Homogenizer (ProScientific) in 200µL to 1ml of 0.1mM ascorbic acid, sonicated 2x5s at 100W and centrifuged (20,000g, 30min, 4°C). Human tissue was homogenized in 1ml of 0.1mM ascorbic acid with a stainless-steel bead Tissue Lyser (Qiagen) during 3min at 30Hz, sonicated 3x10s at 100W with a Digital Sonifier (Banson) and centrifuged (20,000 g, 30min, 4°C). Mouse and Human tissues supernatants were collected and protein concentrations assessed with the Protein Assay kit (Bio-Rad). 20µL of the supernatant was derived with the AccQtag Ultra derivatization kit (Waters). 10µl of each sample was mixed with 30µl of the kit's borate buffer and 10µl of internal standards (10pmol/standard: D5-glutamate, D6-GABA, D5-glycine, C6-noradrenaline, D4-serotonine, D5-HIAA, D4-dopamine and D3-L-DOPA). Then, 10µl of AccQtag reagent was added and the mixture was incubated for 10min at 55°C under stirring. 4 volumes of acetonitrile were added before centrifugation (20,000 *g*, 30min, 4°C). Supernatant was dried and resuspended in 20µl of 99.9% H_2O/0.1% acid formic (v/v). Supernatants were then subjected to LC-MS/MS analysis, performed on a Dionex Ultimate 3000 HPLC system, coupled to an Endura triple quadrupole mass spectrometer (ThermoFisher Scientific) controlled by Xcalibur v.2.0 (Thermo Electron), using the multiple reaction monitoring mode (MRM). 5µl of each sample was loaded onto a ZORBAX SB-C18 Micro Bore Rapid Resolution column (1x150mm, 3.5µm; 90µl/min; Agilent technologies). Identification of the compounds was based on precursor ions, selective fragment ions, and retention times obtained for the neurotransmitters and corresponding internal standards *(88)*. Absolute quantifications of the compounds were done using the ratio of daughter ions response areas on the internal standards according to the isotopic dilution method *(89)*. Amounts of target compounds were normalized to protein concentrations.

Quantitative PCR analysis

Total RNA was extracted using TRIzol reagent (Life Technologies) according to the manufacturer's instructions. 1 µg of RNA was reverse transcribed using the iScripts kit (Bio-Rad). qPCR was performed using SsoAdvanced Universal SYBR Green Supermix on a CFX System (Bio-Rad). Gene expression was normalized using the ΔΔCt method with *Hsp90ab1* and *Gusb* as reference housekeeping genes for WT and *Sod1*^{G86R} and WT and *Fus*$^{\Delta NLS/+}$ samples respectively. The following primer sequences were used for RT-qPCR:

Gusb:	CGAGTATGGAGCAGACGCAA; AGCCTTCTGGTACTCCTCACT
Hsp90ab1:	TACTACTCGGCTTTCCCGTCA; CCTGAAAGGCAAAGGTCTCCA
Adra2a:	TCATCTCCTCGTCCATCGGT; ACGCTTGGCGATCTGGTAAA
Adra2b:	CTGTACCTCCTCCATCGTGC; TACTCCAATGCTCGGCTCAC
Adra2c:	CTGGATCGGCTACTGCAACA; GAAAGAGCGCCTGAAGTCCT
Adrb1:	TTTCTGCAAGGACCCGAGTG; TCCTAGGTGTGGAACCGGAA
Adrb2:	CAGCCATTGCCAAGTTCGAG; GACTAGATCAGCACACGCCA
Comt:	GGGATGAGAGAGTCCTACCAC; AGCAACAGGAGACCCAATGAG
Maoa:	CTGGAGAACGAGCAGCTAGAG; GAGCTGGAACATCCTTGGACT
Maob:	TGGAACCTAGCAAGCAGCAT; GGCCACAATCATGCAGAAGT

Retrograde labelling of LC neurons projecting to the motor cortex

Mice were deeply anesthetized with isoflurane and positioned in a stereotaxic frame, on top of a heating pad. Skin was medially open and the skull was exposed and drilled over the motor area (1mm anterior to Bregma, 1.5mm lateral to the midline) of each hemisphere. A pulled glass micropipet mounted onto a Nanoinjector (Drummond Scientific) was lowered into the cortical parenchyma (-0.75mm) and 500 nl of retrograde AAV-hSyn-eGFP (Addgene, 50465-AAVrg) at $1.53x10^{13}$GC/ml was injected in each hemisphere. Brains were harvested for analyses two weeks after surgery.

Immunofluorescence and image analysis

Mice were euthanized with a lethal i.p. dose of 120 mg/kg of pentobarbital sodium and phenytoin sodium and transcardially perfused with cold 0.01 M PBS, followed by cold 4% PFA in 0.01 M PBS. Brains were dissected and post-fixed overnight in 4% PFA. Brains were cut coronally into 40 µm-thick vibratome sections (Leica Biosystems), and stored at 4°C in 0.01 M PBS with 0.002% Thimerosal until used. Brain and brainstem sections were heated at 80°C in 10 mM citrate buffer for 30 min, incubated 1h in blocking solution (8% goat serum, 0.3% BSA, 0.3% Triton in PBS), and 72 h at 4°C with primary antibodies diluted in the blocking solution. Sections were rinsed, incubated 2 h with the secondary antibodies in blocking solution, rinsed and mounted. The primary antibodies used were: rabbit anti-DBH (Abcam, ab209487, 1/1000), rabbit anti-TH (Millipore, ab152, 1/500), chicken anti-GFP (Rockland, 600-901-215S, 1/500), rabbit anti Alpha 2A (Invitrogen, PA1-048, 1/200), rabbit anti-Alpha 2B (Abcam, ab151727, 1/100), rabbit anti-Alpha 2C (Invitrogen, PA1-4518, 1/100) and rabbit anti-Beta2 adrenoreceptors (Invitrogen MA5-32570, 1/100), rat anti-CTIP2 (Abcam, ab18465, 1/500), mouse anti-parvalbumin (Millipore, MAB1572, 1/1000), mouse anti-somatostatin (Sant Cruz, SC-74556, 1/500). Secondary antibodies (1/1000) were from the Alexa series (1/1000, Life technologies). Images were captured using an AxioImager.M2 microscope equipped with a structured illumination system (Zeiss) and a high-resolution B/W camera (Hamamatsu), and run by the ZEN 2 software (Zeiss). Image analyses were performed with ImageJ software (NIH). For cortical noradrenergic projection analyses, three brain sections were selected (1 mm anterior to Bregma and 0.5 mm and 1.7 mm posterior to Bregma). Noradrenegeric fibre density was quantified as the ratio of DBH-positive area versus the total area of the region of interest. Number and cell surface of TH-positive neurons of the LC were quantified on matched brainstem sections (~5.4 mm posterior to Bregma) and manually counted. Number of GFP-positive neurons were quantified on both sides of 10 following sections matched between genotypes and spanning the rostro-caudal expanse of the LC (~5.350 to 5.750 mm posterior to Bregma). Quantifications were performed by experimenters blinded to the genotype.

Western blot analyses

Motor cortices were homogenized using the Syn-PER Synaptic Protein Extraction kit (Thermo Scientific). Protein concentration was quantitated using the BCA protein assay kit (Pierce). 15µg of proteins were separated on a 4–20% gradient SDS-PAGE gel and transferred on a 0.45µm nitrocellulose membrane using a semi-dry Transblot Turbo system (Bio- Rad). Membranes were saturated with 10% non-fat milk in PBS, and probed with the following above-mentioned primary antibodies against Alpha 2A, Alpha 2B, anti-Alpha 2C and Beta2 adrenoreceptors, diluted at 1/1000 in 3% non-fat milk in PBS. Blots were washed and incubated with anti-Rabbit secondary antibody conjugated with HRP (P.A.R.I.S, BI2407, 1:5000) for 2 hours. Membranes were washed several times and analysed by chemiluminescence using ECL Lumina Forte (Millipore, WBLUF0500) using the Chemidoc XRS Imager (Bio-Rad). Total proteins were detected with a stain-free gel capacity for normalization.

Monitoring noradrenaline release in behaving mice by two-photon imaging

Surgery. Surgical procedures were performed on 60 day-old *SOD1*^{G93A} and at 90 day-old *Fus*$^{\Delta NLS/+}$ mice and their respective non-transgenic littermates as previously described *(20, 90)*. In short, mice were anesthetized using Fentanyl (0.05 mg/kg), Midazolam (5.0 mg/kg), and Metedomidin (0.5 mg/kg) injected intraperitoneally. A 4 mm diameter circular craniotomy, centred at 0.8 mm anterior to Bregma and 1.7 mm lateral from the midline, was performed. AAV2/9-hSyn-GRAB_NE1m (Addgene #123308-AAV9) diluted 1:3 in saline was slowly injected into the primary motor cortex. Three injections (~ 300 nl each, at (1) 2.0 mm lateral and 1.6 mm anterior, (2) 1.7 mm lateral and 0.8 mm anterior to Bregma, and (3) 1.5mm lateral at Bregma) were performed at a cortical depth of 600 µm. The window was then sealed with a 4 mm diameter circular glass coverslip (Warner Instruments) using UV-curable dental acrylic (Venus Diamond Flow, Heraeus Kulzer GmbH). A metal head bar was adhered to the skull by dental acrylic (Paladur, Heraeus Kulzer GmbH) to facilitate stable positioning during in vivo two-photon imaging.

In vivo two-photon imaging in behaving mice. In vivo imaging was conducted four weeks after surgery, and after three days of accustomization of mice to the in vivo setup to minimize stress and arousal responses during recording. GRAB_NE1m was excited at 910nm and imaged within layer II/III in motor cortex. Imaging stacks consisted of 25.000 frames, acquired at 30Hz frame rates (equivalent to ~14 min) with a two-photon microscope (Scientifica, HyperScope, 8 kHz resonant scanner) equipped with a 16x water-dipping objective (Nikon, N16XLWD). Light source was a Ti:Sapphire laser (Spectra Physics MaiTai eHP, with a DeepSee pre-chirp unit). We acquired four to six fields of view (FOV) covering 270x270µm at a resolution of 512x512 pixels in each mouse at cortical depths 200-280µm (4 WT mice [2 females/2 males], 20 FOV; 5 SOD1^{G93A} mice [3 females/2 males)], 20 FOV), at the age of 89.5±0.2 days. During imaging, mice were head-fixed and allowed to run on an air-supported styrofoam ball *(90)* with a pin restricting ball rotation along the pitch axis. Running velocity was tracked using an optical computer mouse sensor *(90)*. To assess the impact of yohimbine on noradrenaline levels during resting/stationary states, the same FOV were repeatedly imaged using the exact same conditions (e.g. laser power) prior to and upon yohimbine treatment.

In vivo imaging data analysis. Analyses were conducted using custom-written routines *(90)* in Matlab 2022a (MathWorks). Brain displacement in x and y was corrected for by full-frame registration. To identify regions of interest (ROIs) we superimposed a grid consisting of small squares (30x30 pixels) on the entire image stack. ROIs were excluded from analysis if the expression level was too low (i.e. mean fluorescence of a given ROI [median intensity of all pixels] was lower than the average of the FOV [median intensity of all pixels] across all frames). The intensity of all pixels in a given ROI was averaged in each frame to generate an NA trace of each ROI. The relative change of fluorescence intensity for each ROI was derived using the following equation:

$\Delta F/F\ ROI = (F_{ROI} - F_{base})/F_{base}$

The baseline (F_{base}) corresponds to the median of the noise band, which was derived by subtracting the 8th percentile within a short sliding window of 3s. Locomotion-associated NA release was assessed only in clear locomotion epochs, characterized by an instantaneous velocity threshold of 1.2 cm/s and an average running speed of 0.3cm/s within 2s after running onset and the absence of any movement within 3s prior to

the selected running onset. NA release was then assessed by computing the area under the curve (AUC) of the NA trace within a window of -0.5 to 1.5s with respect to running onset. Tuning curves were generated by selecting running onsets with defined running velocities (average within 3s upon running onset) for which the corresponding NA response was computed (that is for each velocity bin the maximum value within -0.5 to +1.5s with respect to running onset) was measured. The synchrony of NA release across the FOV was assessed by computing pairwise correlations of all individual ROIs within a FOV.
NA tissue levels during stationary epochs were assessed by normalizing the ROI fluorescence intensity to the background, devoid of the expression of the sensor GRAB-NE, for which reason we divided each ROI intensity by the background value.

Human transcriptomic data
Raw fastq file were obtained from the TargetALS genomic database (https://www.targetals.org/resource/genomic-datasets/). Raw reads were mapped to the human reference genome GRCh38 with STAR version 2.7.0 *(91)* and default parameters using Ensembl gene annotations (version 105). Gene-level abundance estimates were obtained using the option–quantMode geneCount in STAR. We filtered the lowly expressed genes wherein each gene was required to have at least 15 counts across all samples and used both exonic and intronic reads. The filtered set of genes was used for the PCA plot and differential expression analysis. Differential gene expression analysis was performed with the ARMOR workflow *(92)* and a cut off FDR value of 0.05 was set in both datasets. We used post-mortem frontal and motor cortex from controls ($n = 29$) and ALS cases (n=27).

Mouse survival and motor behaviour assessment
The effects of a chronic yohimbine administration (Yoh: 30mg/kg/d, s.c., dissolved in NaCl 0.9% = vehicle, Veh) on disease onset, progression and survival were assessed on *Sod1*^{G86R} mice [n=13 *Sod1*^{G86R} + Veh (5 males and 8 females); 11 *Sod1*^{G86R} + Yoh (4 males and 7 females)] and their WT littermates [n=8 WT + Veh (4 males and 4 females); 11 WT + Yoh (6 males and 5 females)]. Treatment was initiated at 60 days. Mice were trained from 6 weeks of age, and followed from 8 weeks of age until death. General health and neurological symptoms were scored daily as we previously described *(93)*, weight was measured twice a week, and muscle grip strength, inverted grid test and rotarod were performed once a week. Each motor session consisted of three trials and the results represent the mean of these three trials. Each motor session consisted of three trials and the results are presented as the mean of these three trials. Muscle strength was measured on a dynamometer (Bioseb, BIO-GS3). Four limbs hang test during which the mice oppose to their gravitational force was used as previously described *(90)*. Mouse endurance and coordination were measured on a Rotarod (Ugobasil) *(30)*.

Statistics
Data are presented as violin plots with all points, and expressed as average ± SEM. Mouse data statistical analyses, as well as human LC-MS were performed on Prism 6 (GraphPad). Multiple t-tests, one-way or two-way ANOVA, or mixed-effect analyses in the case of missing values, followed by Fischer's LSD multiple comparison *post hoc* tests were used to compare more than two conditions. Two-sided unpaired Student's t-tests were used for comparisons between two conditions, two-sided paired Student's t-tests were used to analyse the PTZ susceptibility and PAC before and after DSP-4 and L-DOPS + Benserazide treatments, and one-sided unpaired Student's t-tests were used for comparisons between two groups of LC-MS human samples. Pearson correlation was used to assess human post-mortem NA concentration against the age at death. Human EEG data analyses were performed on JMP® Pro 16.0.0 (SAS Institute JMP, Brie Comte Robert, France) using a repeated-measures linear mixed-effect model. Multiple regression analyses were performed to test the correlation between MI and patients' clinical features in the same statistical model. Results were considered significant when $p<0.05$.

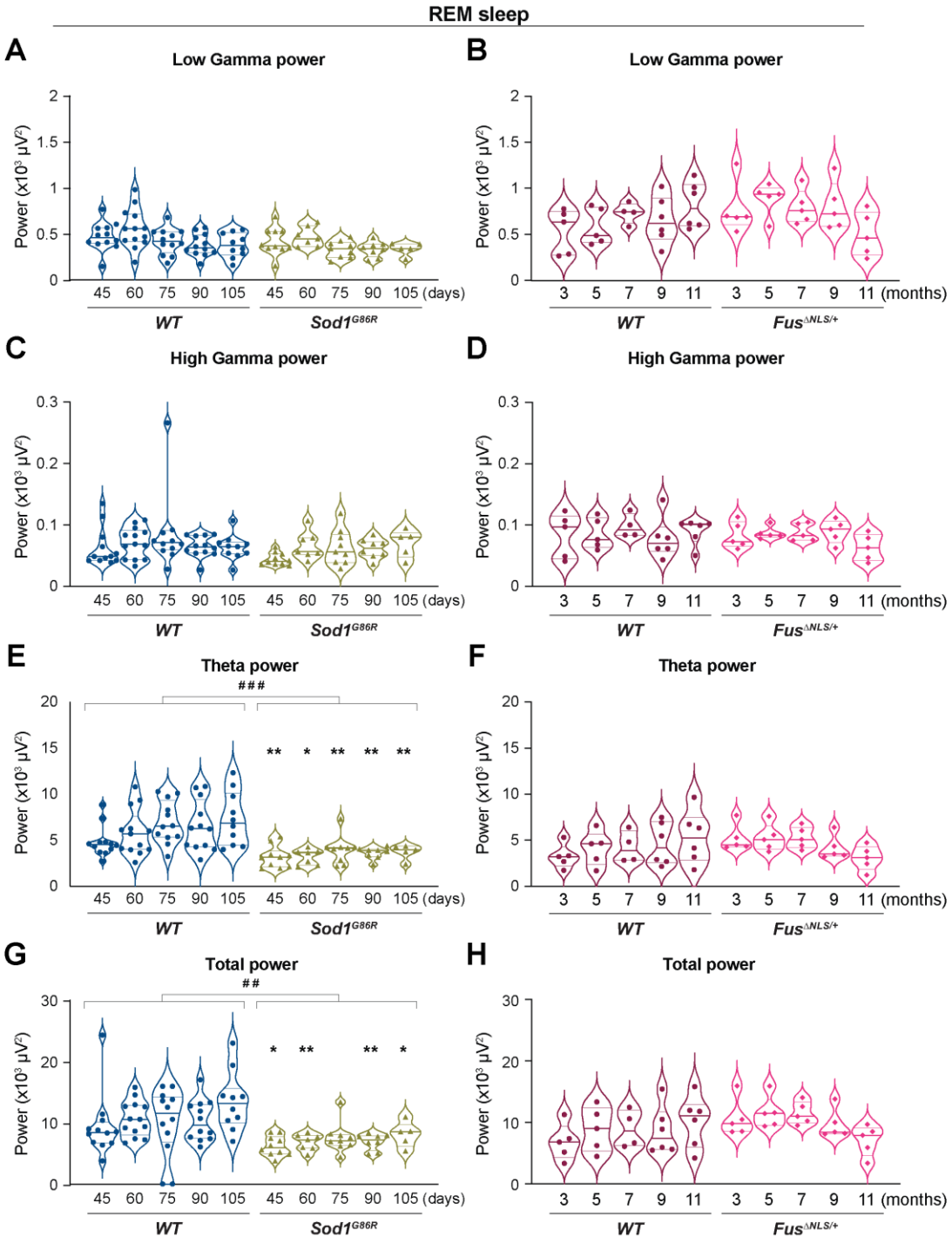

Supplementary Figure 1: Spectral analysis of *Sod1*^{G86R} and *Fus*$^{\Delta NLS/+}$ mice during REM sleep.
(**A-H**) Graphs representing the longitudinal power spectrum analysis of WT and *Sod1*^{G86R} mice and WT and *Fus*$^{\Delta NLS/+}$ mice during REM sleep, including: low gamma power (**A, B**), high gamma power (**C, D**), theta power (**E, F**), and total power (**G, H**). n = 13 WT and 10 *Sod1*^{G86R} mice; n = 6 WT and 5 *Fus*$^{\Delta NLS/+}$ mice. Mixed-effect analysis followed by multiple comparisons test. ##p<0.01 ###p<0.001 for genotype effect in mixed-effect analysis and *p<0.05; **p<0.01; in pairwise comparisons with age-matched WT controls.

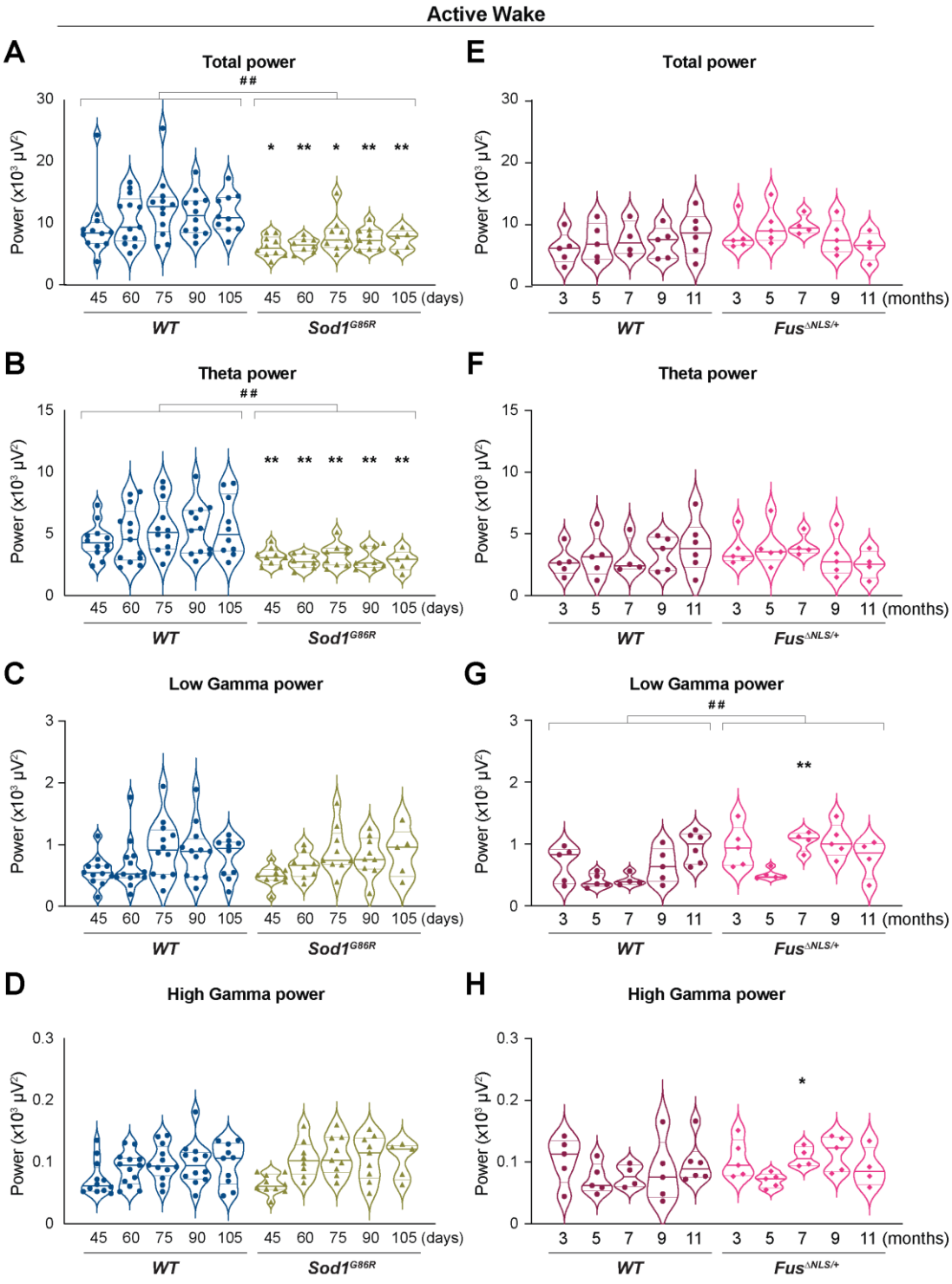

Supplementary Figure 2: Spectral analysis of *Sod1*^{G86R} and *Fus*$^{\Delta NLS/+}$ mice during active wake. (**A-H**) Graphs representing the longitudinal power spectrum analysis of WT and *Sod1*^{G86R} mice (**A-D**) and WT and *Fus*$^{\Delta NLS/+}$ mice (**E-H**) during active wake, including: total power (**A, E**), theta power (**B, F**), low gamma power (**C, G**) and high gamma power (**D, H**). n = 13 WT and 10 *Sod1*^{G86R} mice; n = 6 WT and 5 *Fus*$^{\Delta NLS/+}$ mice. Mixed-effect analysis followed by multiple comparisons test. ##p<0.01 ###p<0.001 for genotype effect in mixed-effect analysis and *p<0.05; **p<0.01; in pairwise comparisons with age-matched WT controls.

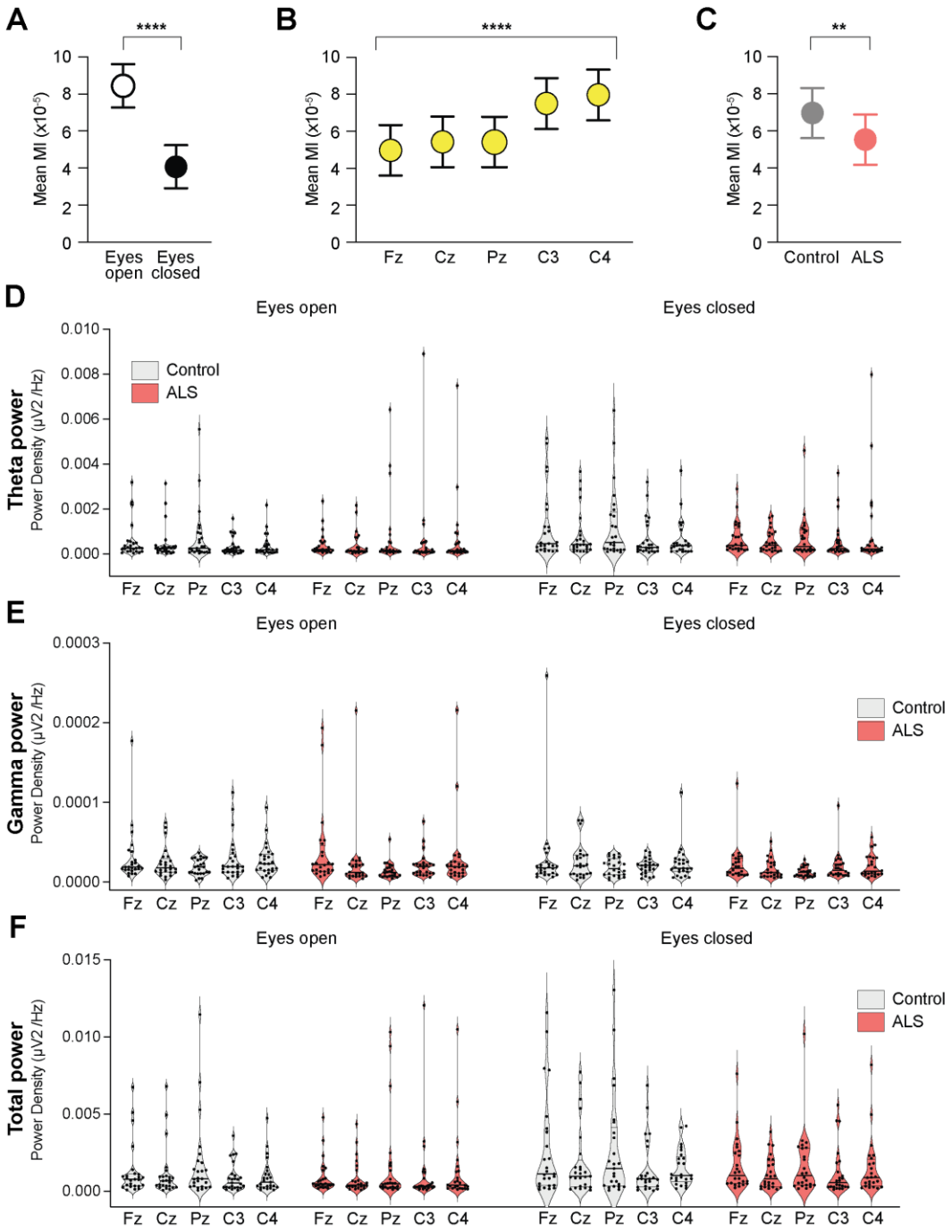

Supplementary Figure 3: rs-EEG recording conditions influences the mean MI of healthy controls and ALS patients, independently from theta, gamma or total powers.

(**A, B, C**) Graphs representing the influence of the recording conditions (EO versus EC, **A**), recording site (channel, **B**), and groups of individuals (Control versus ALS, **C**) on the mean MI. (**D, E, F**) Graphs representing theta (**D**), gamma (**E**) and total (**F**) powers recorded at each of the 5 electrodes of interest (F_Z, C_Z, P_Z, C_3 and C_4) in the EO and EC conditions. n = 26 controls and 26 ALS patients; repeated-measures linear mixed-effect model analysis (rmLMM, **A-F**) with *** $p<0.0001$ and ** $p<0.01$ comparing either the recording conditions, the channels or the group of individuals (**A, B, C**), followed by multiple comparisons test comparing EO and EC conditions, patients and controls in either EO or EC condition, and healthy controls versus ALS patients for a given condition (EO or EC and channel) (**D, F**).

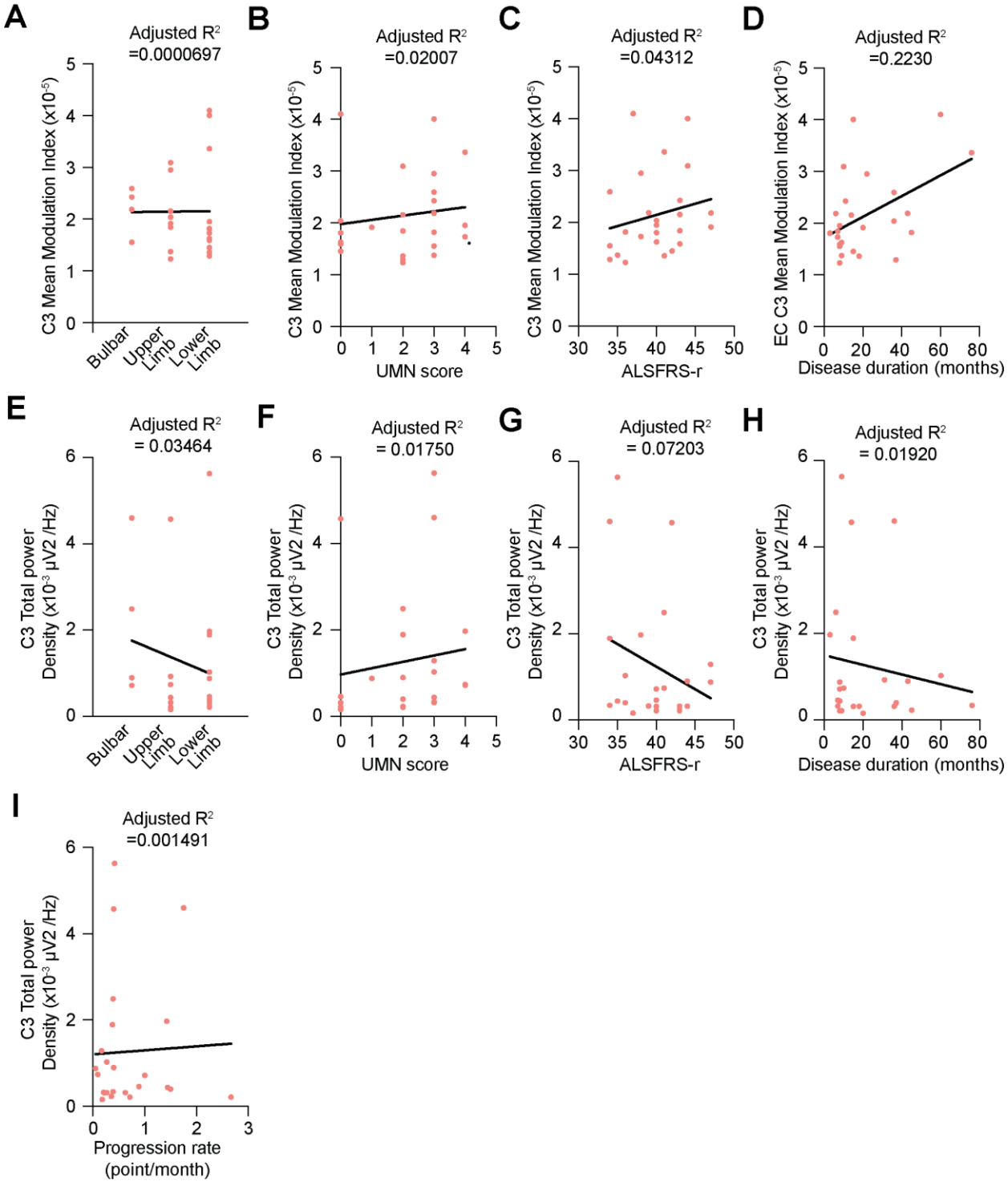

Supplementary Figure 4: Correlation analysis of the mean MI and total power at the level of C3 in sporadic ALS patients and their clinical features in EC rsEEG condition.
(**A-D**) Graphs representing the absence of correlation between the mean MI at the level of C3 of the 26 ALS patients and the site of onset (**A**), upper motor neuron (UMN) score (**B**) ALSFRS-r (**C**) and disease duration (**D**). (**E-I**) Graphs representing the absence of correlation between the total power at the level of C3 of the 26 ALS patients and the site of onset (**E**), UMN score (**F**) ALSFRS-r (**G**), disease duration (**H**) and progression rate (**i**). n = 26 ALS patients; multiple regression analyses.

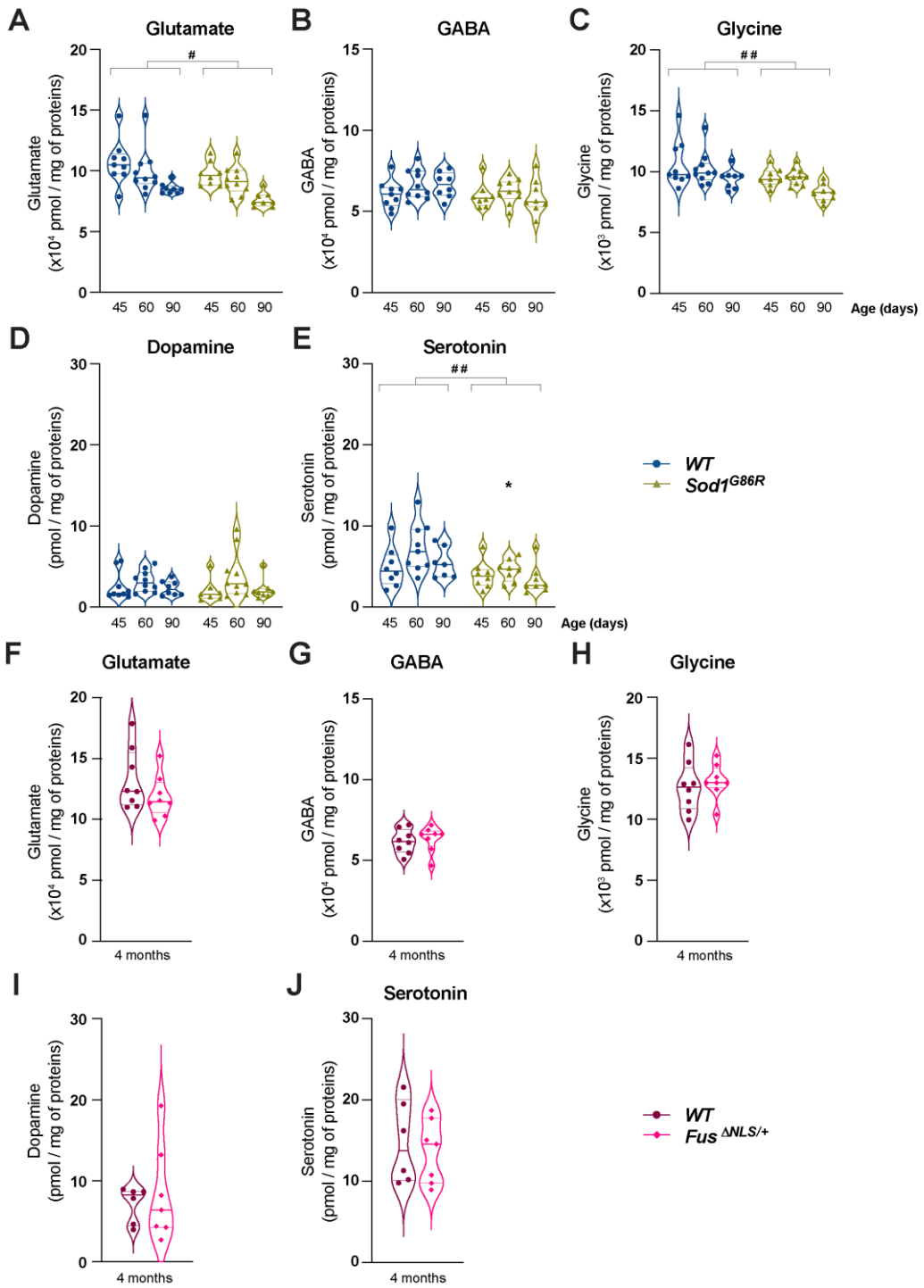

Supplementary Figure 5: LC-MS analysis of the motor cortex of *Sod1*^{G86R} and *Fus*$^{\Delta NLS/+}$ mice.
(**A-J**) Graphs representing the levels of glutamate (**A, F**), GABA (**B, G**), glycine (**C, H**), dopamine (**D, I**) and serotonin (**E, J**) measured by LC-MS in the motor cortex of 45, 60 and 90-day-old *Sod1*^{G86R} (**A-E**) and 4 month-old *Fus*$^{\Delta NLS/+}$ female mice (**F, J**) and their respective controls. n = 9 WT and 8 *Sod1*^{G86R} at 45 days, 10 WT and 10 *Sod1*^{G86R} at 60 days and 8 WT and 8 *Sod1*^{G86R} at 90 days; n = 8 WT and 8 *Fus*$^{\Delta NLS/+}$ at 4 months of age. *Sod1*^{G86R} samples were analysed by two-way ANOVA followed by multiple comparisons test, *Fus*$^{\Delta NLS/+}$ samples were analysed by two-sided unpaired Student's t-test. #p<0.05; ##p<0.01 for genotype effect in two-way ANOVA and *p<0.05 in pairwise comparisons with age-matched WT controls.

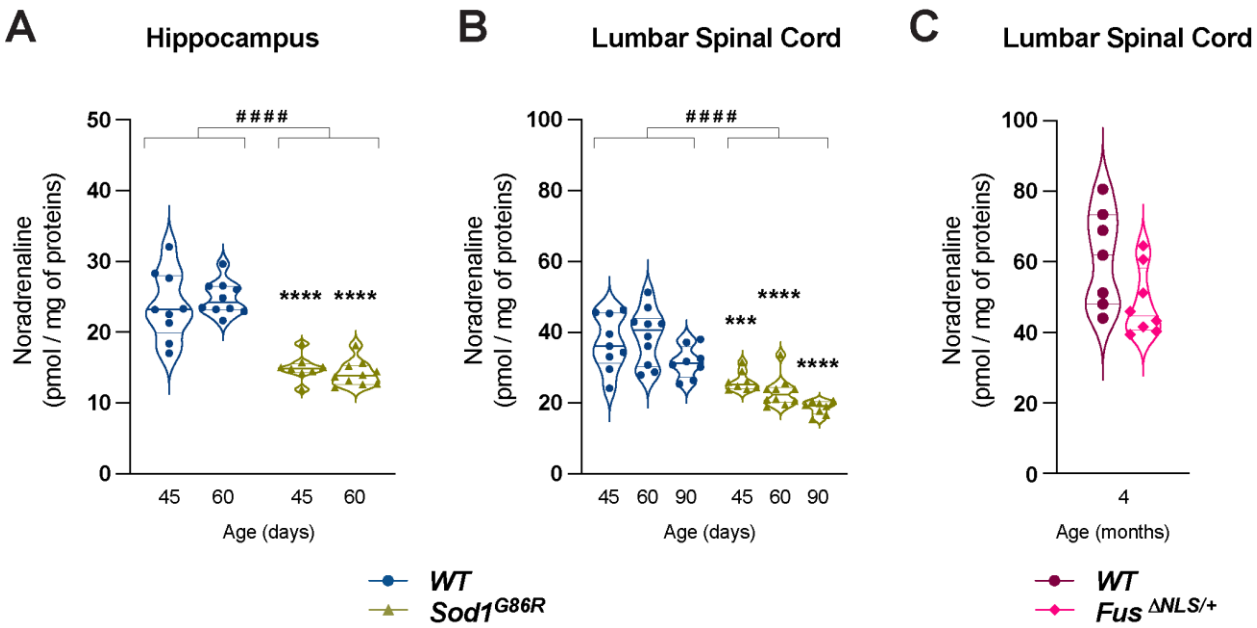

Supplementary Figure 6: LC-MS analysis of the NA levels in the hippocampus and lumbar spinal cord of *Sod1*^{G86R} and *Fus*$^{\Delta NLS/+}$ mice.

(**A-C**) Graphs representing the levels of NA measured by LC-MS in the hippocampus of 45 and 60-day-old *Sod1*^{G86R} female mice and controls (**A**), and in the lumbar spinal of 45, 60 and 90-day-old *Sod1*^{G86R} (**B**) and 4-month-old *Fus*$^{\Delta NLS/+}$ mice (**C**) and their respective controls. n = 9 WT and 8 *Sod1*^{G86R} at 45 days, 10 WT and 10 *Sod1*^{G86R} at 60 days and 8 WT and 8 *Sod1*^{G86R} at 90 days; n = 8 WT and 8 *Fus*$^{\Delta NLS/+}$ at 4 months of age. *Sod1*^{G86R} samples were analysed by two-way ANOVA followed by multiple comparisons test, *Fus*$^{\Delta NLS/+}$ samples were analysed by two-sided unpaired Student's t-test. #### p<0.0001 for genotype effect in two-way ANOVA; *** p<0.001 and ****p<0.0001 in pairwise comparisons with age-matched WT controls.

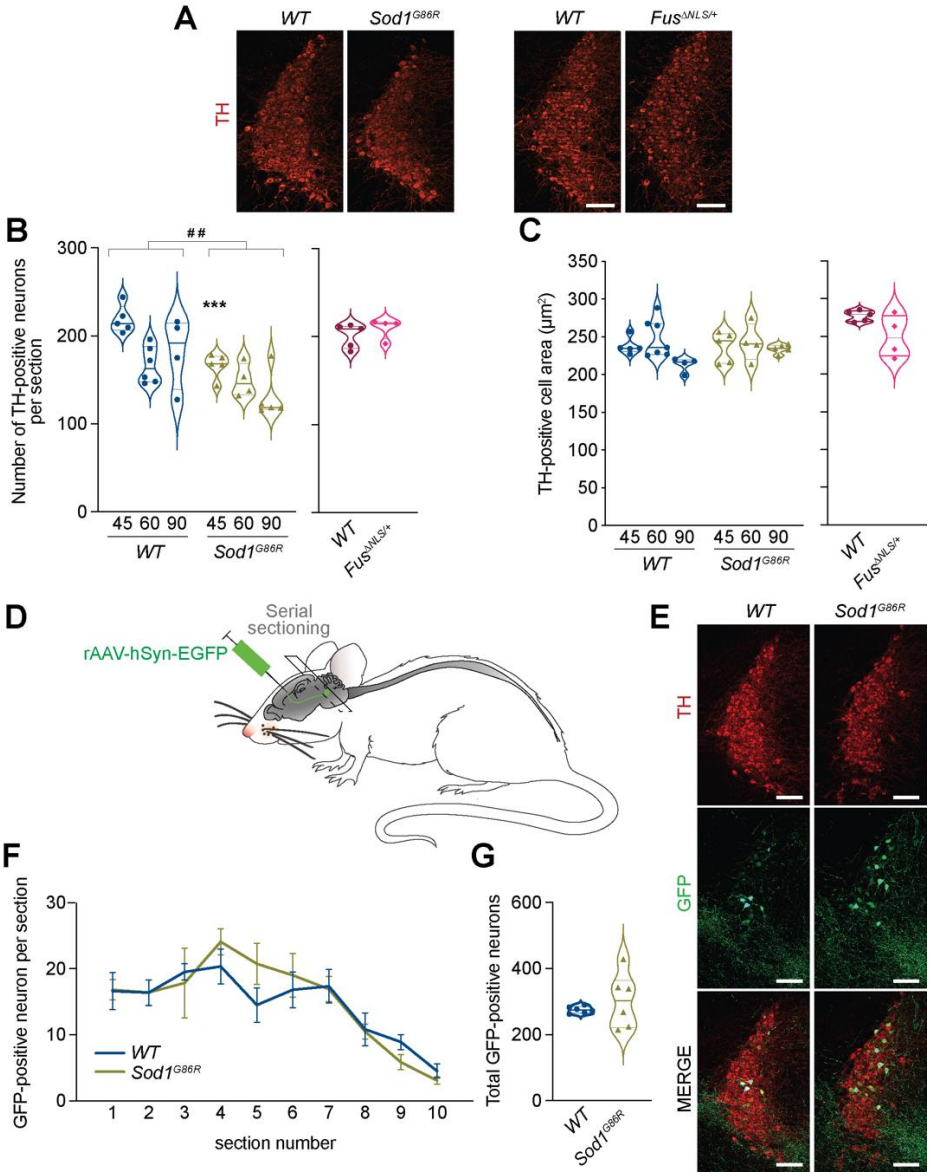

Supplementary Figure 7: Quantification of noradrenergic neurons in the locus coeruleus of *Sod1*^{G86R} and *Fus*$^{\Delta NLS/+}$ mice.

(A) Representative images of coronal section of the brainstem of 45-day-old *Sod1*^{G86R} and 4-month-old *Fus*$^{\Delta NLS/+}$ mice and respective controls showing tyrosine hydroxylase (TH) immunolabelling of the noradrenergic neurons present in the LC. Scale bars = 100 µm. (**B, C**) Quantification of the number (**B**) and cell area (**C**) of TH-positive neurons in the LC of *Sod1*^{G86R} and *Fus*$^{\Delta NLS/+}$ mice and their respective controls. n = 5 WT and 5 *Sod1*^{G86R} at 45 days, 6 WT and 4 *Sod1*^{G86R} at 60 days and 4 WT and 6 *Sod1*^{G86R} at 90 days; n = 5 WT and 4 *Fus*$^{\Delta NLS/+}$ at 4 months of age. (**D**) Schematic representation of the retrograde labelling of noradrenergic neurons from the mouse motor cortex. (**E**) Representative images of coronal section of the brainstem of 90-day-old female *Sod1*^{G86R} mice and controls showing TH and GFP immunolabelling of the noradrenergic neurons. Scale bars = 100 µm. (**F, G**) Quantification of TH- and GFP-positive noradrenergic neurons per coronal hemisection (**F**) or total (**G**) in retrogradelly labelled 85-day-old *Sod1*^{G86R} mice and controls. n = 6 WT and 6 *Sod1*^{G86R} animals). *Sod1*^{G86R} samples were analysed by two-way ANOVA followed by multiple comparisons test (**B, C**), multiple t-test (**F**) and two-sided unpaired Student's t-test (**G**), while *Fus*$^{\Delta NLS/+}$ samples were analysed by two-sided unpaired Student's t-test. ##p<0.01 for genotype effect in two-way ANOVA and ***p<0.001 in pairwise comparisons with age-matched WT controls.

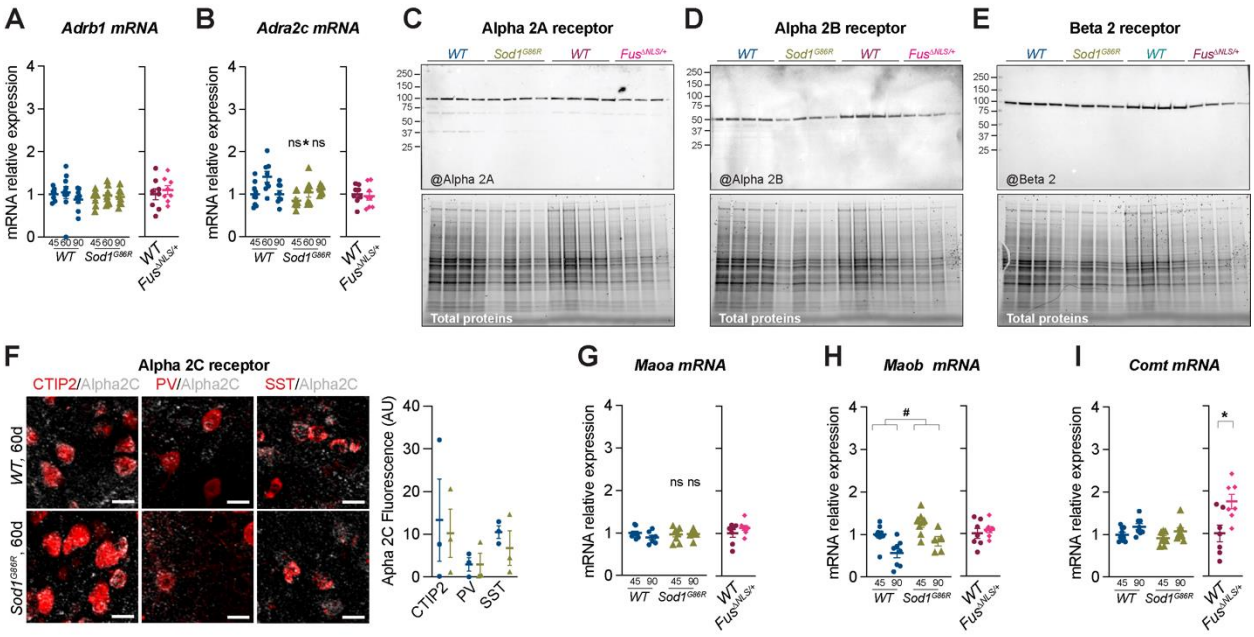

Supplementary Figure 8: Relative protein and mRNA expression of noradrenergic components in the motor cortex of *Sod1*^{G86R} and *Fus*$^{\Delta NLS/+}$ mice.

(**A, B**) Graphs representing the relative mRNA expression levels of *Adra2c* and *Adrb1* in the motor cortex of 45, 60 and 90-day-old *Sod1*^{G86R} and 4-month-old *Fus*$^{\Delta NLS/+}$ mice and their respective controls. n = 9 WT and 8 *Sod1*^{G86R} at 45 days, 10 WT and 10 *Sod1*^{G86R} at 60 days, and 8 WT and 8 *Sod1*^{G86R} at 90 days; n = 7 WT and 7 *Fus*$^{\Delta NLS/+}$. (**C, D, E**) Representative western blot images (top) revealing Alpha 2A, 2B and B2 adrenoreceptors in motor cortex extracts from 90-day-old *Sod1*^{G86R} and 6-month-old *Fus*$^{\Delta NLS/+}$ mice and their respective controls (n=4 female mice per group), along with the corresponding stain-free gels used for protein normalization (bottom). (**F**) Representative images of the cerebral cortex (left) of 60-day-old WT and *Sod1*^{G86R} mice upon immunolabelling to reveal adrenergic receptors 2C (white) along with CTIP2-, PV- and SST-positive neurons (red)., scale bars: 10 µm, and quantification (right) of the adrenergic receptors 2C in CTIP2-, PV- and SST-positive neurons (n=3 female mice per group). (**G, H, I**) Graphs representing the relative mRNA expression levels of *Maoa, Maob* and *Comt,* in the motor cortex of 45, 60 and 90-day-old *Sod1*^{G86R} and 4-month-old *Fus*$^{\Delta NLS/+}$ mice and their respective controls. n = 9 WT and 8 *Sod1*^{G86R} at 45 days, 10 WT and 10 *Sod1*^{G86R} at 60 days, and 8 WT and 8 *Sod1*^{G86R} at 90 days; n = 7 WT and 7 *Fus*$^{\Delta NLS/+}$. *Sod1*^{G86R} samples were analysed by two-way ANOVA followed by multiple comparisons test, *Fus*$^{\Delta NLS/+}$ samples were analysed by two-sided unpaired Student's t-test. #p<0.05; for genotype effect in two-way ANOVA and *p<0.05 in pairwise comparisons with age-matched WT controls.

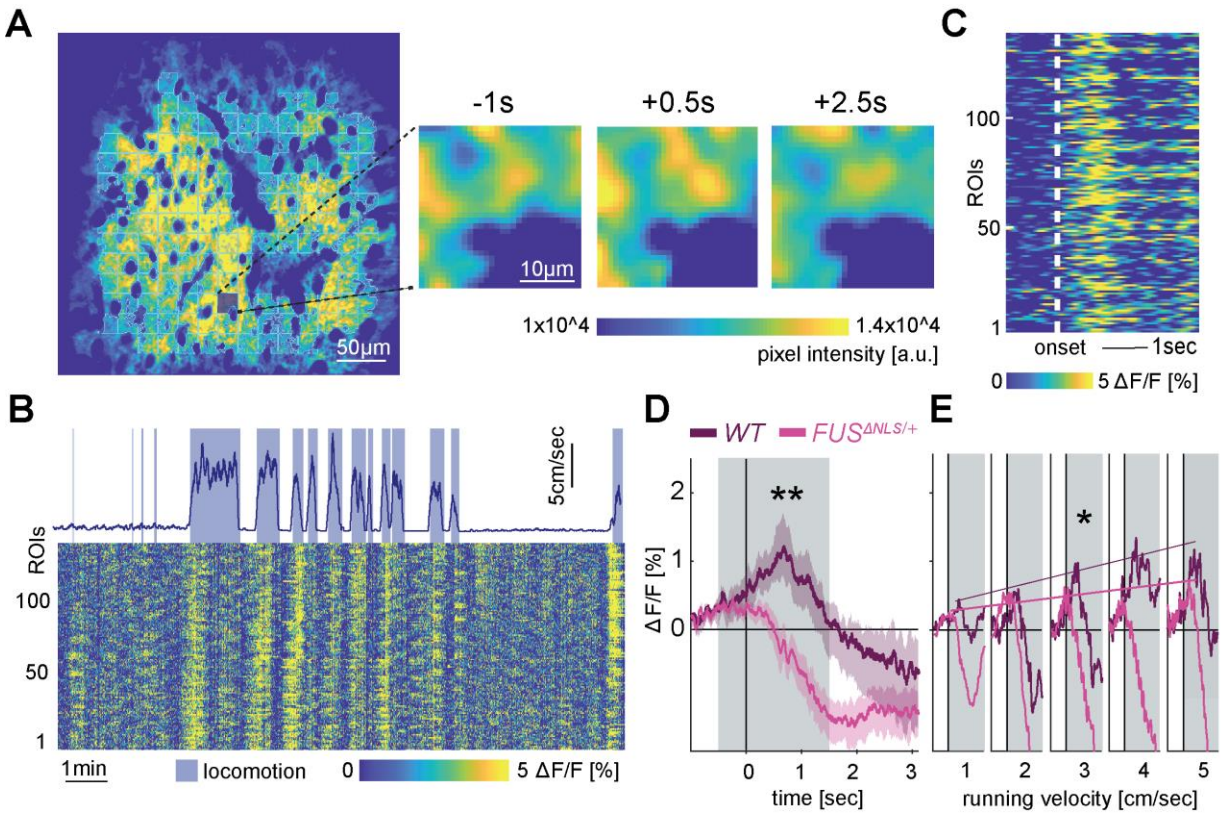

Supplementary Figure 9: Release of NA is reduced in behaving *Fus*$^{\Delta NLS/+}$ mice.
(**A**) Representative mean projection of a field of view (FOV) displaying the expression of the GRAB-NE1m indicator for NA. Superimposed grid demonstrates location and size of regions of interest (ROIs). Insert and images on the right show change in fluorescence with locomotion onset of a selected ROI (time with respect to locomotion onset). (**B**) Heat map of fluorescent traces of all ROIs in an example FOV across the entire recording session referenced by running speed (blue trace on top) and binary running epochs (blue area). (**C**) Averaged running-associated response of each ROI for the same FOV shown in (b). (**D**) Average population response to locomotion onset of all FOVs in *WT* (brown) and *Fus*$^{\Delta NLS/+}$ mice (pinke) (p=0.0084, Wilcoxon rank sum test for the area under the curve [grey area], *WT*: 17 FOV, 2 male and 4 female mice; *Fus*$^{\Delta NLS/+}$: 21 FOV, 2 male and 3 female mice). (**E**) Speed-dependent tuning curve of the locomotion-associated NA release (linear fit of the maximum values within –0.5 to 1.5 s of running onset in each velocity bin, grey area) in WT (y=0.638x + 0.004, R^2=0.862) and *Fus*$^{\Delta NLS/+}$ mice (y=0.219x + 0.005, R^2=0.313), intercept difference between WT and *Fus*$^{\Delta NLS/+}$ p=0.0462, One-way ANOVA). Scale bar in (a) 50µm, high magnification images 10µm. *p<0.05, **p<0.01.

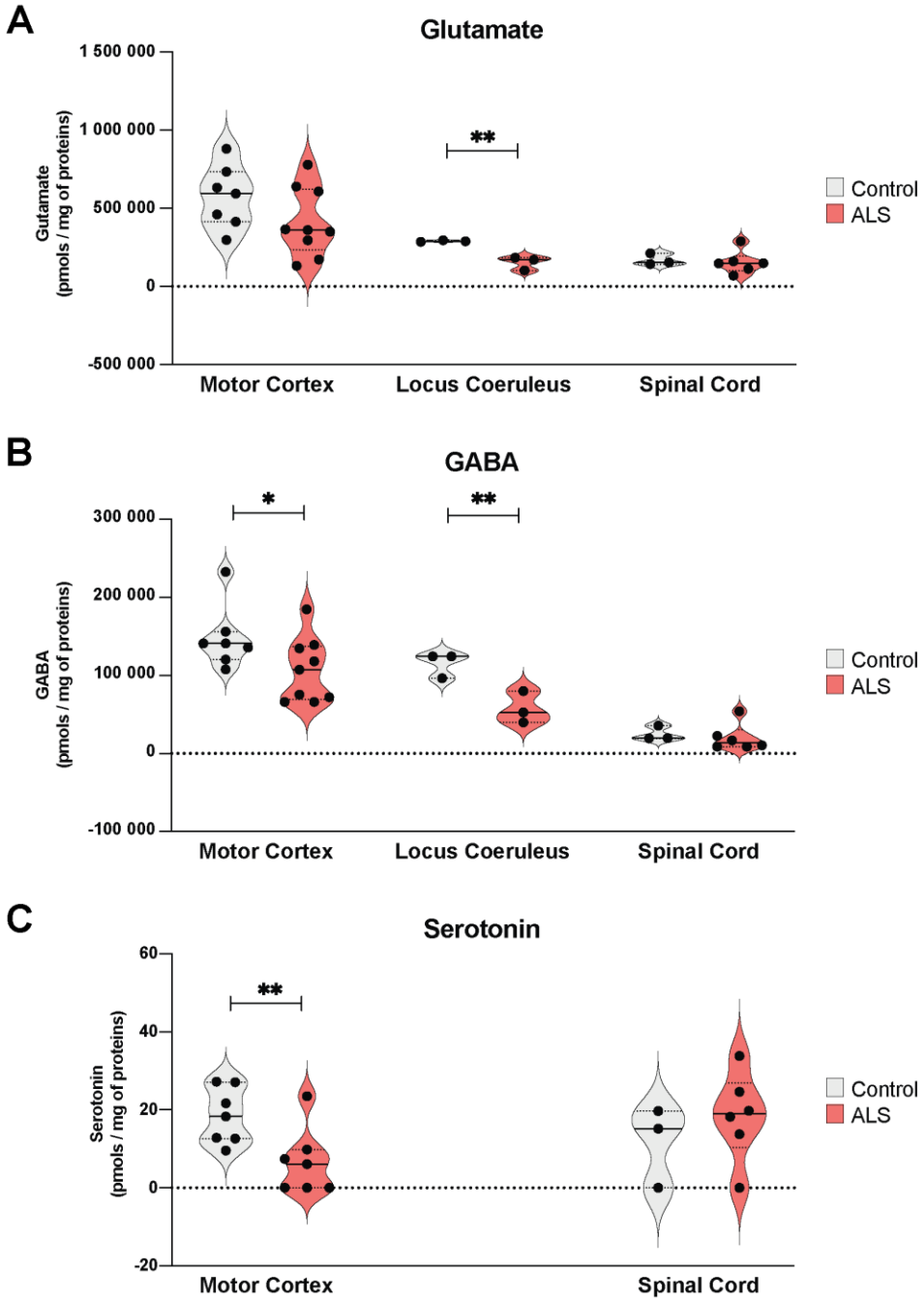

Supplementary Figure 10: LC-MS analysis of the neurotransmitter levels in post-mortem motor cortex, locus coeruleus and spinal cord from ALS patients.

(**A-C**) Graphs representing the levels of glutamate (**A**), GABA (**B**) and serotonin (**C**) measured by LC-MS in post-mortem motor cortex, LC and spinal cord from ALS patients. Motor cortex: n = 7 healthy controls, 9 ALS patients; LC: n = 3 healthy controls, 3 ALS patients; spinal cord n = 3 healthy controls, 6 ALS patients. One-sided unpaired Student's t-test. *p<0.05; **p<0.01.

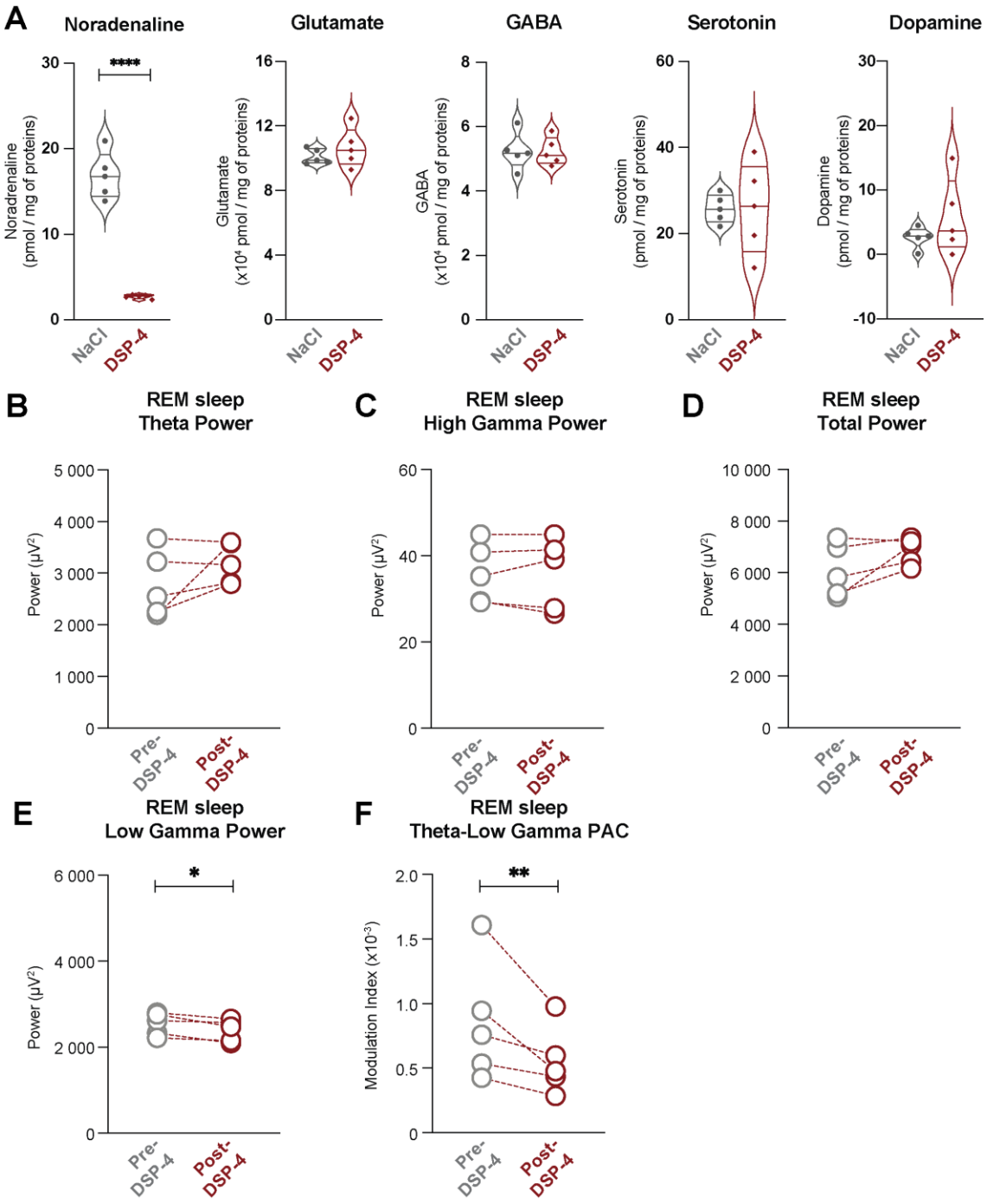

Supplementary Figure 11: Effect of DSP-4 administration on the cortical levels of neurotransmitters and on spectral powers and PAC during REM sleep in WT mice.

(**A**) Graphs representing the levels of NA, glutamate, GABA, serotonin and dopamine measured by LC-MS in the motor cortex of WT animals 8 days after DSP-4 or control NaCl injection. n=5 WT + NaCl and 5 WT + DSP-4; two-sided unpaired Student's t-test; ****p<0.0001; ns: non-significant. (**B-E**) Before-after graphs representing the spectrum analysis of theta (**B**), high gamma (**C**), total (**D**) and low gamma (**E**) powers prior to (grey circles) and 8 days after (red circles) DSP-4 administration. (**F**) Before-after graph representing the MI of theta-low gamma PAC during REM sleep before (grey circles) and after (red circles) DSP-4 administration. n=5 WT animals; two-sided paired Student's t-test; *p<0.05; **p<0.01.

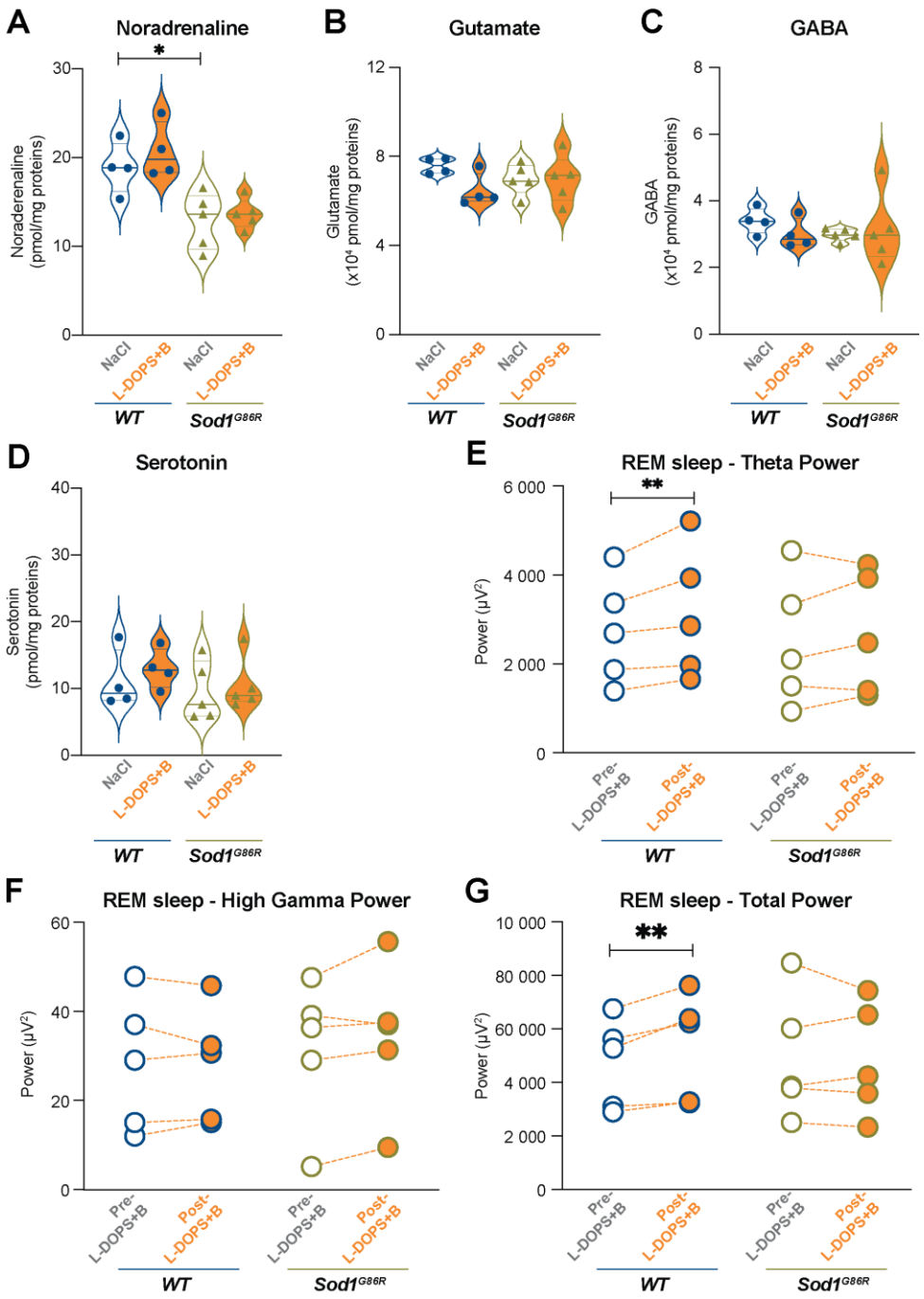

Supplementary Figure 12: Effect of L-DOPS and benserazide administration on the cortical levels of neurotransmitters and spectral powers during REM sleep in WT and *Sod1*^{G86R} mice.

(**A-D**) Graphs representing the levels of NA (**A**), glutamate (**B**), GABA (**C**), and serotonin (**D**) measured by LC-MS in the motor cortex of WT animals, 8 hrs after L-DOPS and benserazide (L-DOPS+B) injection or control saline solution (NaCl). n=4 WT + NaCl, 4 WT + L-DOPS+B and 5 *Sod1*^{G86R} + NaCl, 5 *Sod1*^{G86R} + L-DOPS+B; two-sided unpaired Student's t-test; *p<0.05; ns: non-significant. (**E-G**) Before-after graphs representing the spectrum analysis of theta (**E**), high gamma (**F**) and total (**G**) powers during REM sleep prior to (empty circles) and 12 hours after (filled yellow circles) L-DOPS+B administration to WT (blue circles) and *Sod1*^{G86R} (green circles) animals. n=5 WT and 5 *Sod1*^{G86R} mice; two-sided paired Student's t-tests; **p<0.01.

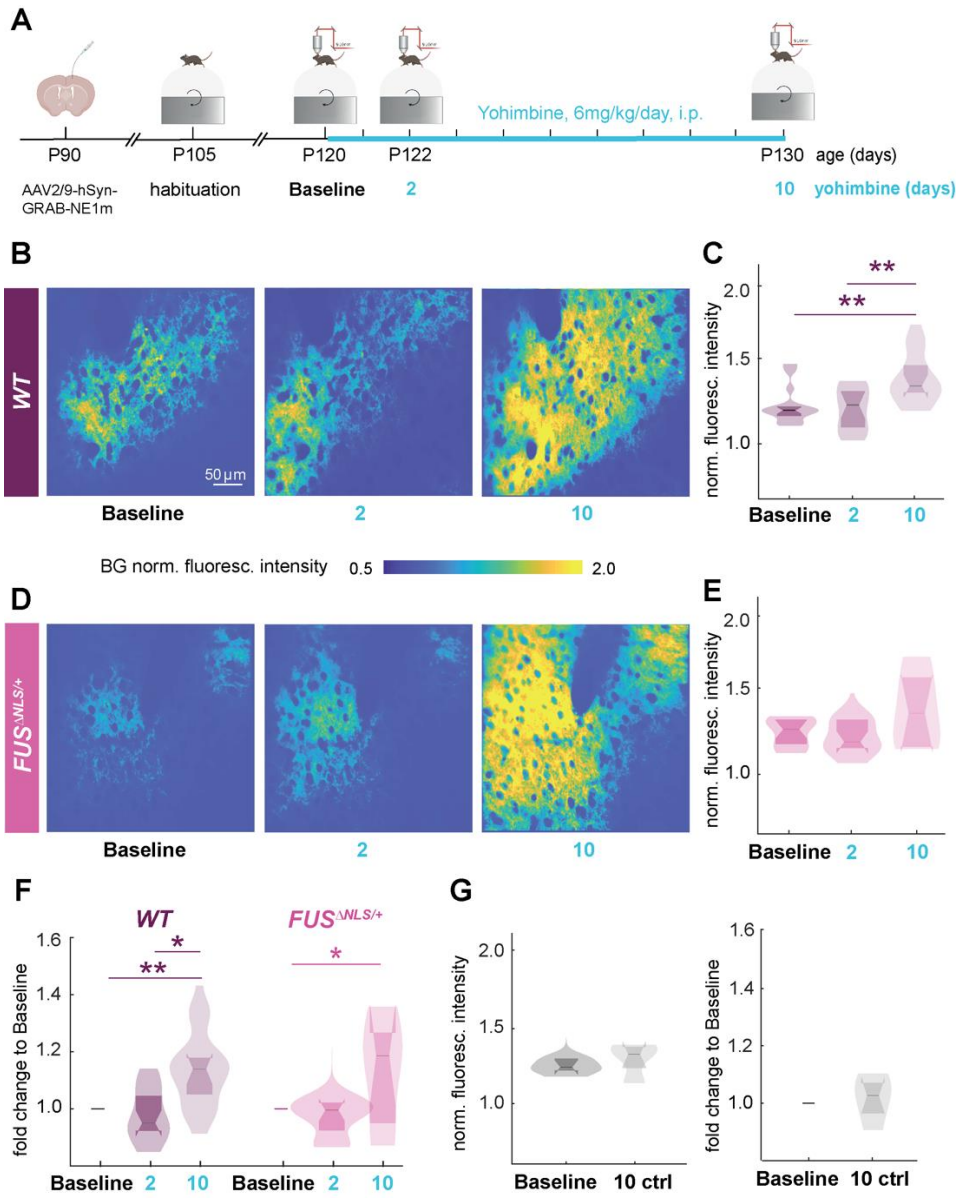

Supplementary Figure 13: Cortical NA levels during stationary states are elevated upon yohimbine treatment.

(**A**) Experimental timeline *Fus*$^{\Delta NLS/+}$ mice. (**B**) Representative mean projection of stationary epochs of a field of view (FOV) in a WT mouse illustrating the fluorescence intensity of the GRAB-NE1m indicator of NA before yohimbine treatment ('Baseline'), after two days of yohimbine ('2') and 10 days of yohimbine ('10'). (**C**) Quantification of GRAB-NE1m fluorescence normalized to the background (BG) signal in WT mice (Baseline vs day 10: p=0.002; day 2 vs day 10: p=0.0047) (Baseline, day 2: n = 18 FOV, 2 male, 3 female mice; day 10: n=12 FOV, 2 male, 3 female mice). (**D**) Same as in (b) for a 4-month-old *Fus*$^{\Delta NLS/+}$ mouse. (**E**) As in (c) for *Fus*$^{\Delta NLS/+}$ (Baseline, day 2: n=11 FOV; 2 male, 2 female mice; day 10: n=8 FOV; 2 male, 1 female mice). (**F**) Fold change of the fluorescence intensity in *WT* (Baseline vs day 10 p=0.0027, day 2 vs day 10 p=0.0047) and in *Fus*$^{\Delta NLS/+}$ (Baseline vs day 10 p=0.022, day 2 vs day 10 p=0.092, all Wilcoxon rank sum tests). (**G**) Quantification of GRAB-NE1m fluorescence intensities during stationary epochs in control mice (ctrl) not receiving any yohimbine applications (left, Baseline vs day 10 control, p=0.54) and the fold change of this signal in individual FOV (right, p=0.69, n=7 FOV, 3 females). Scale bar in (b) 50µm *p<0.05, **p<0.01.

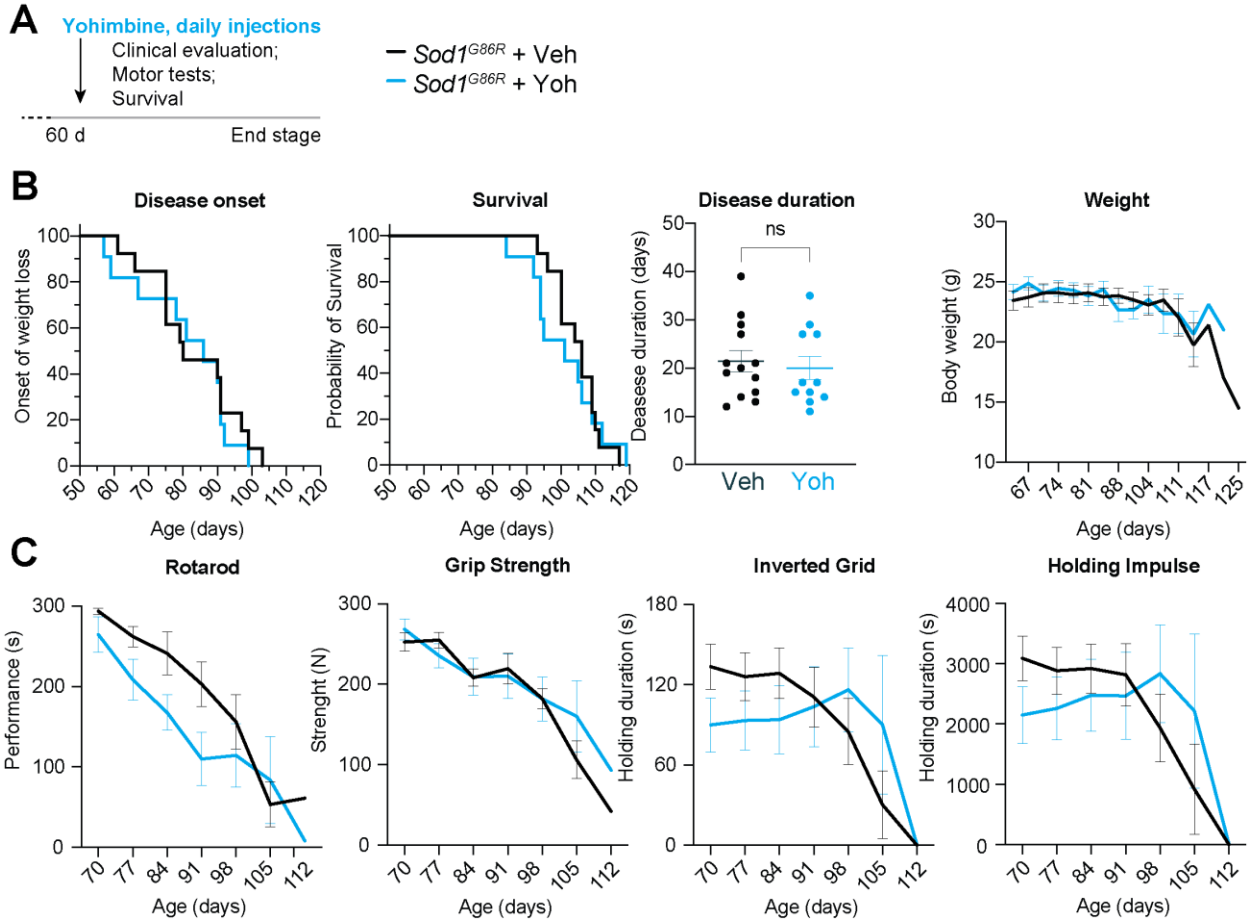

Supplementary Figure 14: Chronic yohimbine administration does not modify symptoms onset and progression in *Sod1*^{G86R} mice.

(**A**) Design of the experiment. *Sod1*^{G86R} mice were subjected to daily subs-cutaneous injections of yohimbine (Yoh) at a dose of 30mg/kg or of vehicle (Veh, 0.9% NaCl in water) from 60 days on. Their weight was measured twice a week and motor performances evaluated once a week by the mean of rotarod, grip tests and inverted grid test. (**B**) Yohimbine did not modify disease onset (estimated as the onset of weight loss), survival, disease duration or weight evolution of the animals. (**C**) Yohimbine did not modify motor performances evaluated by the duration of the runs on the rotarod, muscular strength, holding time or impulse on the inverted grid test. n=13 *Sod1*^{G86R} + Veh (5 males and 8 females); 11 *Sod1*^{G86R} + Yoh (4 males and 7 females). Log-rank Mantel-Cox tests (onset and survival), two-tailed unpaired t-test (disease duration), mixed effect analyses (weight and motor performances). No significant difference was found.

Case	Gender	Age	PMD	MC	LC	SC
Ctl 1	M	100	n.p.	x	x	x
Ctl 2	M	85	n.p.	x	x	x
Ctl 3	M	95	n.p.	x	x	x
Ctl 4	F	80	16.67	x		
Ctl 5	F	67	27-28	x		
Ctl 6	M	42	42	x		
Ctl 7	F	76	n.p.	x		
ALS 1	F	55	n.p.	x	x	x
ALS 2	F	61	23	x	x	x
ALS 3	M	59	n.p.	x	x	x
ALS 4	M	69	31	x	x	x
ALS 5	M	54	14	x		x
ALS 6	M	74	27	x		x
ALS 7	F	70	39	x		
ALS 8	F	78	62	x		
ALS 9	M	72	6.83	x		

Supplementary table 1: Subjects included in the LC-MS study.
M: male; F: female; PMD: post-mortem delay; MC: motor cortex; LC: locus coeruleus; SC: spinal cord; n.p.: not provided.